

The second RIT binary black hole simulations catalog and its application to gravitational waves parameter estimation

James Healy, Carlos O. Lousto, Jacob Lange, Richard O’Shaughnessy, Yosef Zlochower, and Manuela Campanelli

*Center for Computational Relativity and Gravitation,
School of Mathematical Sciences, Rochester Institute of Technology,
85 Lomb Memorial Drive, Rochester, New York 14623*

(Dated: March 29, 2019)

The RIT numerical relativity group is releasing the second public catalog of black-hole-binary waveforms <http://ccrg.rit.edu/~RITCatalog>. This release consists of 320 accurate simulations that include 46 precessing and 274 nonprecessing binary systems with mass ratios $q = m_1/m_2$ in the range $1/7 \leq q \leq 1$ and individual spins up to $s/m^2 = 0.95$. The new catalog contains search and ordering tools for the waveforms based on initial parameters of the binary, trajectory information, peak radiation, and final remnant black hole properties. The final black hole remnant properties provided here can be used to model the merger of black-hole binaries from its initial configurations. The waveforms are extrapolated to future null infinity and can be used to independently interpret gravitational wave signals from laser interferometric detectors. As an application of this waveform catalog we reanalyze the signal of GW150914 implementing parameter estimation techniques that make use of only numerical waveforms without any reference to information from phenomenological waveforms models.

PACS numbers: 04.25.dg, 04.25.Nx, 04.30.Db, 04.70.Bw

I. INTRODUCTION

Ten years of advances and studies since the breakthroughs [1–3] in numerical relativity led to detailed predictions of the gravitational waves from the late inspiral, plunge, merger, and ringdown of black-hole-binary systems (BHB). These predictions helped to accurately identify the first direct detection [4] of gravitational waves with such binary black hole systems [5–8] and match them to targeted supercomputer simulations [9–11]. The observed gravitational waves were remarkably consistent with the predictions of numerical general relativity [7, 8, 12], thereby supporting the notion that general relativity is an accurate theory of gravity in the highly dynamical, strong field regime of merging binary black holes.

Numerical relativity techniques have been used to explore the late dynamics of spinning black-hole binaries, beyond the post-Newtonian regime for several years. The first generic, long-term precessing black-hole binary evolutions (i.e., without any symmetry) were performed in Ref. [13], where a detailed comparison with post-Newtonian $\ell = 2, 3$ waveforms was made. More recently, the longest of such comparisons for a precessing binary was done in [14] and a full numerical simulation was performed for a nonspinning binary with 350 orbits in Ref. [15].

Numerical simulations have started to explore the corners of parameter space, these include near extremal [16] with $\chi = 0.99$ spinning black-hole binaries in Refs. [17, 18], mass ratios as small as $q = 1/100$ in Refs. [19, 20], and large initial separations, $R = 100M$, in Ref. [21]. Similarly challenging, high energy collision of black holes were studied in Ref. [22–24] and hyperbolic

black-hole encounters in Ref. [25, 26].

Other important studies include the exploration of the *hangup* effect, i.e. the role individual black-hole spins play to delay or accelerate their merger [27–30], the determination of the magnitude and direction of the *recoil* velocity of the final merged black hole [31–38], and the *flip-flop* of individual spins during the orbital phase [14, 39, 40], as well as precession dynamics [41–45] and the inclusion of those dynamics to construct surrogate models for gravitational waveforms [46–48].

There have been several significant efforts to coordinate numerical relativity simulations to support gravitational wave observations. These include the numerical injection analysis (NINJA) project [49–52], the numerical relativity and analytical relativity (NRAR) collaboration [53], and the waveform catalogs released by the SXS collaboration [54–56], Georgia Tech. [57], and RIT [58].

In this paper we describe a new release of the public waveform catalog by the RIT numerical relativity group that nearly triples the number of waveforms by adding a new set of 194 waveforms, with 154 aligned spins and 40 precessing binaries. The catalog has new search and ordering features and includes all modes $\ell \leq 4$ modes of ψ_4 and the strain h (both extrapolated to null-infinity). The catalog can be accessed from <http://ccrg.rit.edu/~RITCatalog>.

This paper is organized as follows. In Section II we describe the methods and criteria for producing the numerical simulations and evaluation of their errors in order to be included in the RIT catalog. In Sec. III we describe the use of the new searching and ordering capabilities of all the relevant BHB parameters, the file format, and the full content of the data in the catalog. In Sec. IV we use the waveform catalog to estimate the binary black

hole parameters that best match the first gravitational wave event GW150914. We use the Bayesian likelihood maximized over extrinsic parameters as described in [59] and map it onto the grid of simulations. Use of interpolation routines lead to an estimate of the confidence intervals that are consistent with previous estimates for the aligned spin binaries. We conclude in Sec. V with a discussion of the future use of this catalog for parameter inference of new gravitational waves events and the extensions to this work to more generic precessing binaries.

II. FULL NUMERICAL EVOLUTIONS

The simulations in the RIT Catalog were evolved using the LAZEv code [60] implementation of the moving puncture approach [2] (with the modifications suggested by Ref. [61]). In all cases (except the very high spin where we use CCZ4 [62]) we use the BSSNOK (Baumgarte-Shapiro-Shibata-Nakamura-Oohara-Kojima) family of evolutions systems [63–65]. For the runs in the catalog, we used a variety of finite-difference orders, Kreiss-Oliger dissipation orders, and Courant factors [66–68]. All of these are given in the metadata included in the catalog and the references associated with each run (where detailed studies have been performed).

The LAZEv code uses the EINSTEINTOOLKIT [69, 70] / CACTUS [71] / CARPET [72] infrastructure. The CARPET mesh refinement driver provides a “moving boxes” style of mesh refinement. In this approach, refined grids of fixed size are arranged about the coordinate centers of both holes. The code then moves these fine grids about the computational domain by following the trajectories of the two black holes (BHs).

We use AHFINDERDIRECT [73] to locate apparent horizons. We measure the magnitude of the horizon spin using the *isolated horizon* (IH) algorithm detailed in Ref. [74] (as implemented in Ref. [75]). Once we have the horizon spin, we can calculate the horizon mass via the Christodoulou formula $m_H = \sqrt{m_{\text{irr}}^2 + S_H^2}/(4m_{\text{irr}}^2)$, where $m_{\text{irr}} = \sqrt{A/(16\pi)}$ and A is the surface area of the horizon.

To compute the numerical initial data, we use the puncture approach [76] along with the TWOPUNCTURES [77] code. To compute initial low eccentricity orbital parameters, we use the post-Newtonian techniques described in [78] to determine quasi-circular orbits. We then evaluate the residual eccentricity during evolution via the simple formula, as a function of the separation of the holes, d , $e_d = d^2 \ddot{d}/M$, as given in [13].

As discussed in Ref. [58] the main sources of numerical errors in this catalog are due to finite difference truncation, finite extraction radii, finite number of modes, and the non-zero residual initial eccentricities and displacement of the center of mass.

During the early inspiral, the irreducible masses and intrinsic spins of each black hole should be nearly con-

stant because the levels of gravitational wave energy and momentum absorbed by the holes is 4–5 orders of magnitude smaller[79] than those emitted to infinity. During a simulation, the masses and spins vary due to numerical truncation error, and we then use these variations as a measure of the size of the truncation error. For our current simulations we monitor accuracy by measuring the conservation of the individual horizon masses and spins during evolution, as well as the level of satisfaction of the Hamiltonian and momentum constraints, to ensure reaching an accuracy consistent with our main applications. Those measurements are seen to be preserved at least to one part in 10^4 in the cases of the masses and one part in 10^3 in the cases of the spins (see for instance Fig. 6 in Ref. [45]).

We measure radiated energy, linear momentum, and angular momentum, in terms of the radiative Weyl Scalar ψ_4 , using the formulas provided in Refs. [80, 81]. These formulas are strictly speaking only valid on future null-infinity (\mathcal{I}^+). We therefore measure the radiated energy-momentum on a series of timelike worldtubes of finite radius and then extrapolate to $r = \infty$ using both linear and quadratic extrapolations. The difference between these two extrapolations is an estimate for the uncertainty.

Unlike the radiated energy-momentum, more care is needed to properly extrapolate the waveform itself to \mathcal{I}^+ . As described in Ref. [82], we use the Teukolsky equation to obtain expressions for $r\psi_4$ at \mathcal{I}^+ based on its values on a timelike worldtube traced out by a fixed sphere of constant (large) areal radius r [see Eq. (29), there]. The expressions there contain the corrections of order $\mathcal{O}(1/r)$ and $\mathcal{O}(1/r^2)$ to $r\psi_4$. As shown in Ref. [82], this extrapolation is consistent with both the waveform and the radiated energy-momentum extrapolated using a least squares fit to a polynomial in $1/r$. Additionally, the $\mathcal{O}(1/r)$ perturbative corrections were shown to be consistent with a Cauchy-Characteristic extraction for an equal-mass binary in [83].

Various simulations in this catalog were studied in detail in previous papers. In Appendix A of Ref. [84], we performed a detailed error analysis of configurations with equal mass and spins aligned/antialigned with respect to the orbital angular momentum; in Appendix B of Ref. [68], we performed convergence studies for runs with mass ratios ($q = 1, 3/4, 1/2, 1/3$) and measured errors due to finite observer locations; and in Ref. [85], we performed convergence studies for $q \geq 1/10$ nonspinning binaries.

Finally, in addition to all the internal consistency analysis and error estimates, in Ref. [11] we showed that for the parameter estimated for GW150914 ($q = m_1/m_2 = 0.82$ and spins for the small/large holes of $\chi_1 = -0.44$ and $\chi_2 = +0.33$), the RIT waveforms and those produced completely independently by the SXS collaboration have an excellent match [86] of $\gtrsim 0.99$ overall for modes up to $\ell = 5$. In Ref. [87] a similar agreement between approaches has been found for five targeted precessing and nonprecessing simulations of GW170104, displaying a 4th

order convergence with finite difference resolution. The comparisons were also carried up to $\ell = 5$ -modes. For all modes up to $l \leq 4$ we found a match of $\gtrsim 0.99$ and $\gtrsim 0.97$ for the $l = 5$ modes.

In all our studies we concluded that the waveforms at the resolutions provided in this catalog are well into the convergence regime (roughly converging at 4th-order with resolution), that the horizon evaluated quantities such as the remnant final mass and spins have errors of the order of 0.1%, and that the radiatively computed quantities such as the recoil velocities and peak luminosities are evaluated at a typical error of 5%.

III. THE CATALOG

The RIT Catalog can be found at <http://ccrg.rit.edu/~RITCatalog>. Figure 1 shows the distribution of the non-precessing runs in the catalog in terms of $\chi_{1,2}$ and q (where χ_i is the component of the dimensionless spins of BH i along the direction of the orbital angular momentum). The information currently in the catalog consists of the metadata describing the runs and all modes up through the $\ell = 4$ modes (enough for most applications) of $M\psi_4$ extrapolated to \mathcal{I}^+ via the perturbative approach of [82]. The associated metadata include the initial orbital frequencies, ADM masses, initial waveform frequencies from (2,2) mode, black hole masses, momenta, spins, separations, and eccentricities, as well the black-hole masses and spins once the initial burst of radiation has left the region around the binary. Note that we normalize our data such that the sum of the two initial horizon masses is $1M$. These *relaxed* quantities (at $t_{\text{relax}} = 200M$ after the initial burst of radiation has mostly dissipated) are more accurate and physically relevant for modeling purposes. In addition, we also include the final remnant black hole masses, spins and recoil velocity.

The catalog is organized using an interactive table [88] that includes an identification number, resolution, type of run (nonspinning, aligned spins, precessing), the initial proper length of the coordinate line joining the two BH centroids that is outside both horizons [21], the coordinate separation of the two centroids, the mass ratio of the two black holes, the components of the dimensionless spins of the two black holes, the starting waveform frequency, $Mf_{22,\text{relax}}$, time to merger, number of gravitational wave cycles calculated from the (2,2) modes from the beginning of the inspiral signal to the amplitude peak, remnant mass, remnant spin, recoil velocity, peak luminosity, amplitude and frequency. The final column gives the appropriate bibtex keys for the relevant publications where the waveforms were first presented. The table can be sorted (ascending or descending) by any of these columns. And there is a direct search feature that runs over all table elements.

Resolutions are given in terms of the grid spacing of the refinement level where the waveform is extracted

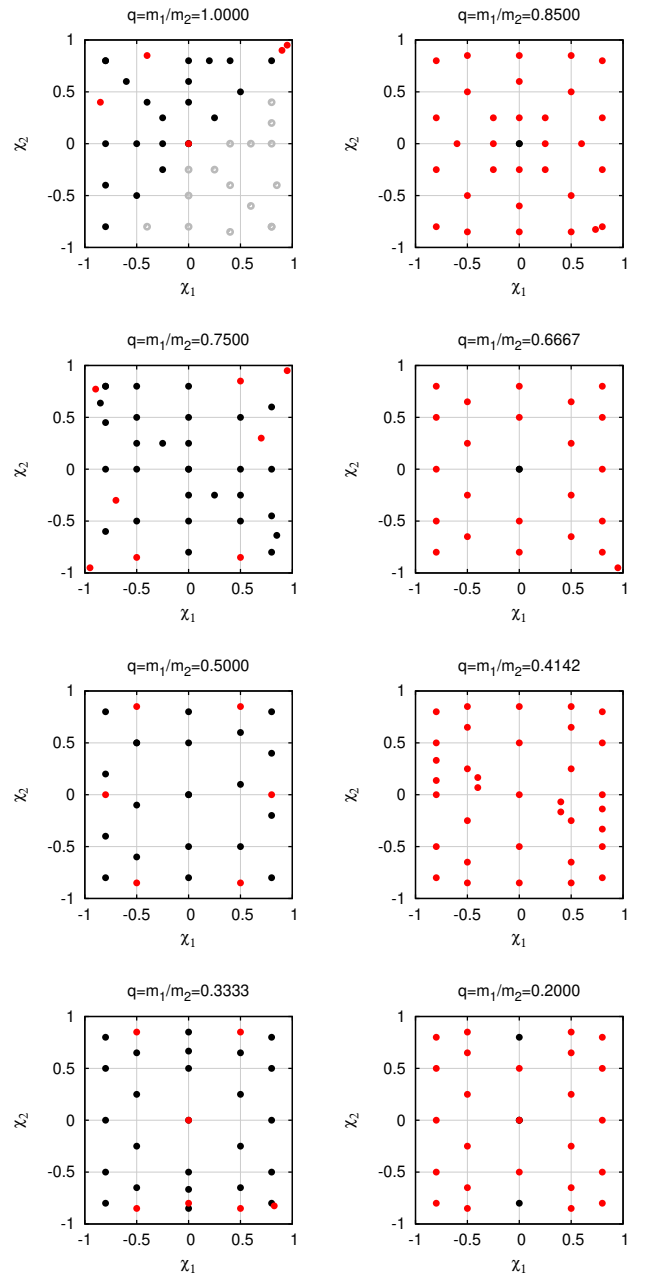


FIG. 1. Initial parameters in the (q, χ_1, χ_2) space for the 274 nonprecessing binaries. Note that χ_i denotes the component of the dimensionless spin of BH i along the orbital angular momentum. Each panel corresponds to a given mass ratio that covers the comparable masses binary range from $q = 1$ to $q = 1/5$. The dots in black denote the simulations of the catalog first release, and the dots in red are those of this second release.

(which is typically two refinement levels below the coarsest grid) with $R_{\text{obs}} \sim 100M$. We use the notation nXY, where the grid spacing in the wavezone is given by $h = M/X.YY$, e.g., n120 corresponds to $h = M/1.2$.

For each simulation in the catalog there are three files: one contains the metadata information in ASCII format,

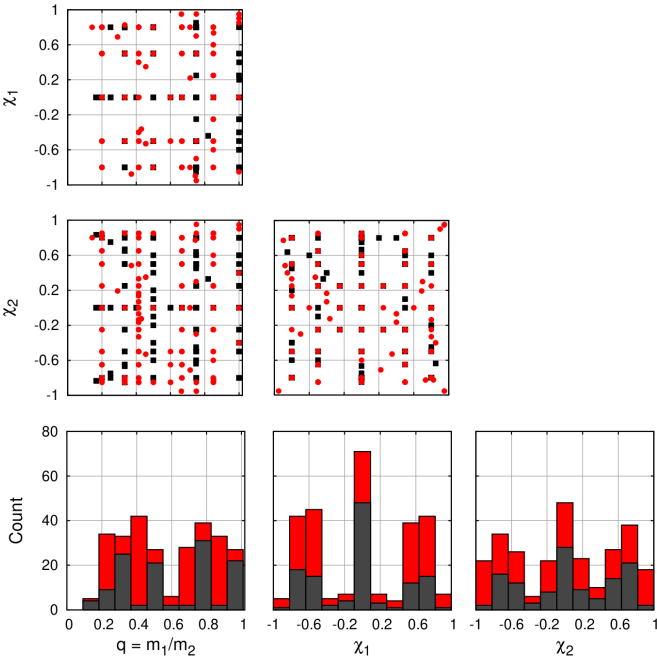


FIG. 2. Counting simulations in the (q, χ_1, χ_2) planes (faces of the cube) for the 274 nonprecessing binaries. The 120 release 1 simulations are black and the 154 release 2 simulations are red.

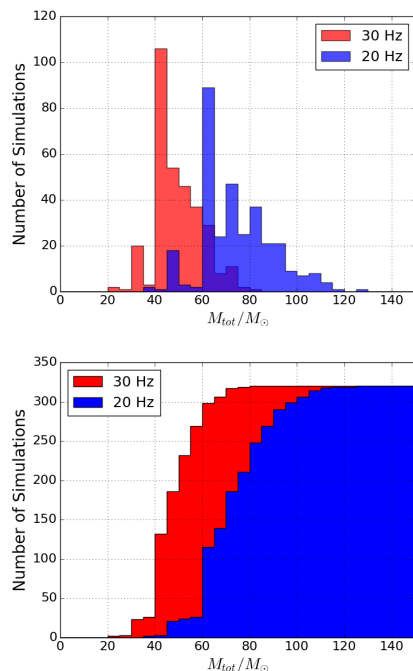


FIG. 3. Top: Distributions of the total mass of BHB systems in the RIT catalog corresponding to a starting gravitational wave frequency of 20 Hz (blue) and 30 Hz (red) in bins of $5M_\odot$. Bottom: The cumulative version of the above plot also in bins of $5M_\odot$ for the 320 simulations in this catalog.

the other two are a tar.gz files containing ASCII files with up to and including $\ell = 4$ modes of $Mr\psi_4$ and h . In the near future, data will be available in the Numerical Relativity Injection format [89]. Note that the primary data in our catalog is the Weyl scalar $Mr\psi_4$ extrapolated to \mathcal{I}^+ (using Eq. (29) of Ref. [82]), rather than the strain $(r/M)h$. We provide the strain but also leave it to the user to convert $Mr\psi_4$ to strain for most modes since this is still a sensitive process and is best handled on a mode-by-mode basis. The subtleties associated with transforming ψ_4 to h arise from the two integrations required [13, 90]. One of the standard techniques, developed in Ref. [91], performs this integration in Fourier space with a windowing function and a low-frequency cutoff. Both of these require fine-tuning of parameters. The codes to do this are open-source and publicly available from <https://svn.einsteintoolkit.org/pyGWAnalysis/trunk>.

Figure 2 shows the distribution of the 274 nonprecessing runs in the catalog in terms of $\chi_{1,2}$ and q . Those runs were motivated by systematic studies to produce a set of accurate remnant formulas to represent the final mass, spin and recoil of a merged binary black hole system and the peak Luminosity, amplitude and frequency, as a function of the parameters of the precursor binary, as reported in [30, 68, 84]. A second important motivation was to provide a grid of simulations for parameter estimation of gravitational wave signals detected by LIGO using the methods described in [9]. We will see in the next section that we have achieved a good coverage of this BHB parameter space.

The precessing runs in the catalog were motivated to study particular spin dynamics of merging BHB, such as the study of unstable spin flip-flop, as reported in [40] and the targeted followups of gravitational wave signal from the first and second LIGO observing runs [11, 87]. We have also payed special attention to the systematic study of simulations covering a 4-dimensional parameter space involving a spinning and a nonspinning black hole binary as a function of the mass ratio. Those simulations were originally performed to study remnant recoil and final masses and spins [92]. We have supplemented them here with additional 31 simulations to have a coverage of spin orientations (see Table II that allows an estimation of precession as shown in Fig. 8).

Figure 3 shows the distributions of the minimal total mass of the BHB systems in the catalog given a starting gravitational wave frequency of 20 or 30 Hz in the source frame. This provides a coverage for the current events observed by LIGO (redshift effects improve this coverage by a factor of $1 + z$, where z is the redshift). Coverage of even lower total masses would require longer simulations or hybridization of the current waveforms with Post-Newtonian methods [51].

IV. APPLICATION OF THE CATALOG TO PARAMETER ESTIMATION OF BINARY BLACK HOLES

We can directly compare any of our simulations to real or synthetic gravitational wave observations by scaling that simulation and its predictions to a specific total redshifted mass M_z and then marginalizing the likelihood for the gravitational wave data over all extrinsic parameters [9, 93–96]: the seven coordinates characterizing the spacetime coordinates and orientation of the binary relative to the earth. Specifically the likelihood of the data given Gaussian noise has the form (up to normalization)

$$\ln \mathcal{L}(\boldsymbol{\lambda}; \theta) = -\frac{1}{2} \sum_k \langle h_k(\boldsymbol{\lambda}, \theta) - d_k | h_k(\boldsymbol{\lambda}, \theta) - d_k \rangle_k - \langle d_k | d_k \rangle_k, \quad (1)$$

where h_k are the predicted response of the k^{th} detector due to a source with parameters $(\boldsymbol{\lambda}, \theta)$ and d_k are the detector data in each instrument k ; $\boldsymbol{\lambda}$ denotes the combination of redshifted mass M_z and the remaining intrinsic parameters (mass ratio and spins; with eccentricity ≈ 0) needed to uniquely specify the binary's dynamics; θ represents the seven extrinsic parameters (4 spacetime coordinates for the coalescence event and 3 Euler angles for the binary's orientation relative to the Earth); and $\langle a | b \rangle_k \equiv \int_{-\infty}^{\infty} 2df \tilde{a}(f)^* \tilde{b}(f) / S_{h,k}(|f|)$ is an inner product implied by the k^{th} detector's noise power spectrum $S_{h,k}(f)$. In practice we adopt a low-frequency cutoff f_{\min} so all inner products are modified to

$$\langle a | b \rangle_k \equiv 2 \int_{|f| > f_{\min}} df \frac{[\tilde{a}(f)]^* \tilde{b}(f)}{S_{h,k}(|f|)}. \quad (2)$$

Fig. 5 displays the error estimates of the aligned spins and mass ratio binary parameters for GW150914 at 90%, 95% (2σ), and 99.7% (3σ) confidence levels. Note that the diagonal shape of higher likelihoods the first panel is in part inherited by the symmetry of the $q = 1$ case, given that the binary has comparable masses. The elongated (with bubbles) diagonal shape of the first panel translates into a vertical shapes in the last two panels.

The 90% confidence level gives

$$\begin{aligned} 0.570 < q &< 1.00, \\ 0.00 < |\chi_1| &< 1.00, \\ 0.00 < |\chi_2| &< 0.78, \\ -0.44 < \chi_{\text{eff}} &< 0.14, \\ -0.44 < S_{hu} &< 0.14, \\ 66.3 < M_{total} &< 79.2 \end{aligned}$$

Where M_{total} is given in solar mass M_{\odot} units.

Compare these values to the GW150914 properties pa-

For our analysis of GW150914, we adopt the same noise power spectrum employed in previous work [9, 96]. After exploring a range of redshifted masses M_z for each simulation, we estimate $\ln \mathcal{L}(M_z)$ as a function of mass for that simulation and thus in particular its maximum value $\ln \mathcal{L}_{\max}$, as in [9, 94].

A. Non-precessing binaries

Fig. 4 displays a likelihood map for the simulations as a function of black hole's individual spins, with a panel for each of the eight mass ratios studied, $q = 1.00, 0.85, 0.75, 0.6667, 0.4142, 0.50, 0.3333, 0.20$ on both LIGO detectors, H1 and L1, combined. Our priors of intrinsic parameters are the discrete set of numerical relativity simulations (q, χ_1, χ_2) , with 100 points in uniform spacing between $40 < M_{total}/M_{\odot} < 120$. The heat maps are generated using a multiquadric radial basis interpolating function $\sqrt{(D/\epsilon)^2 + 1}$ between the computed likelihoods for each simulation plotted by hollow circles (D being the distance of the point in parameter space and $\epsilon = 0.25$). We have options for using different interpolating functions, among them Gaussian process regression. The results are all compatible and the differences decrease with the increased number of simulations. We also tested the consistency of the results by dropping randomly 10% of the simulations used to produce the interpolated maps. Note that we have restricted the grids to spin magnitudes ≤ 0.85 in order to produce interpolation maps and avoid at this stage extrapolations to larger spins until we produce enough simulations in the ≥ 0.85 region.

per [4]

$$\begin{aligned} 0.62 < q &< 0.99, \\ 0.04 < |\chi_1| &< 0.90, \\ 0.03 < |\chi_2| &< 0.78, \\ -0.29 < \chi_{\text{eff}} &< 0.1, \\ 66.1 < M_{total} &< 75.2 \end{aligned}$$

Fig. 6 displays a comparative analysis of the single spin approximations to aligned binaries using a linear interpolation. The upper panel presents our preferred variables for the spin, S_{hu}

$$m^2 S_{hu} = \left(\left(1 + \frac{1}{2q} \right) \vec{S}_1 + \left(1 + \frac{1}{2}q \right) \vec{S}_2 \right) \cdot \hat{L}, \quad (3)$$

to describe the leading effect of hangup on the waveforms [30]. The lower panel displays a comparative heatmap using the common approximate model variable [97]

$$m^2 \chi_{\text{eff}} = \left(\left(1 + \frac{1}{q} \right) \vec{S}_1 + \left(1 + q \right) \vec{S}_2 \right) \cdot \hat{L}.$$

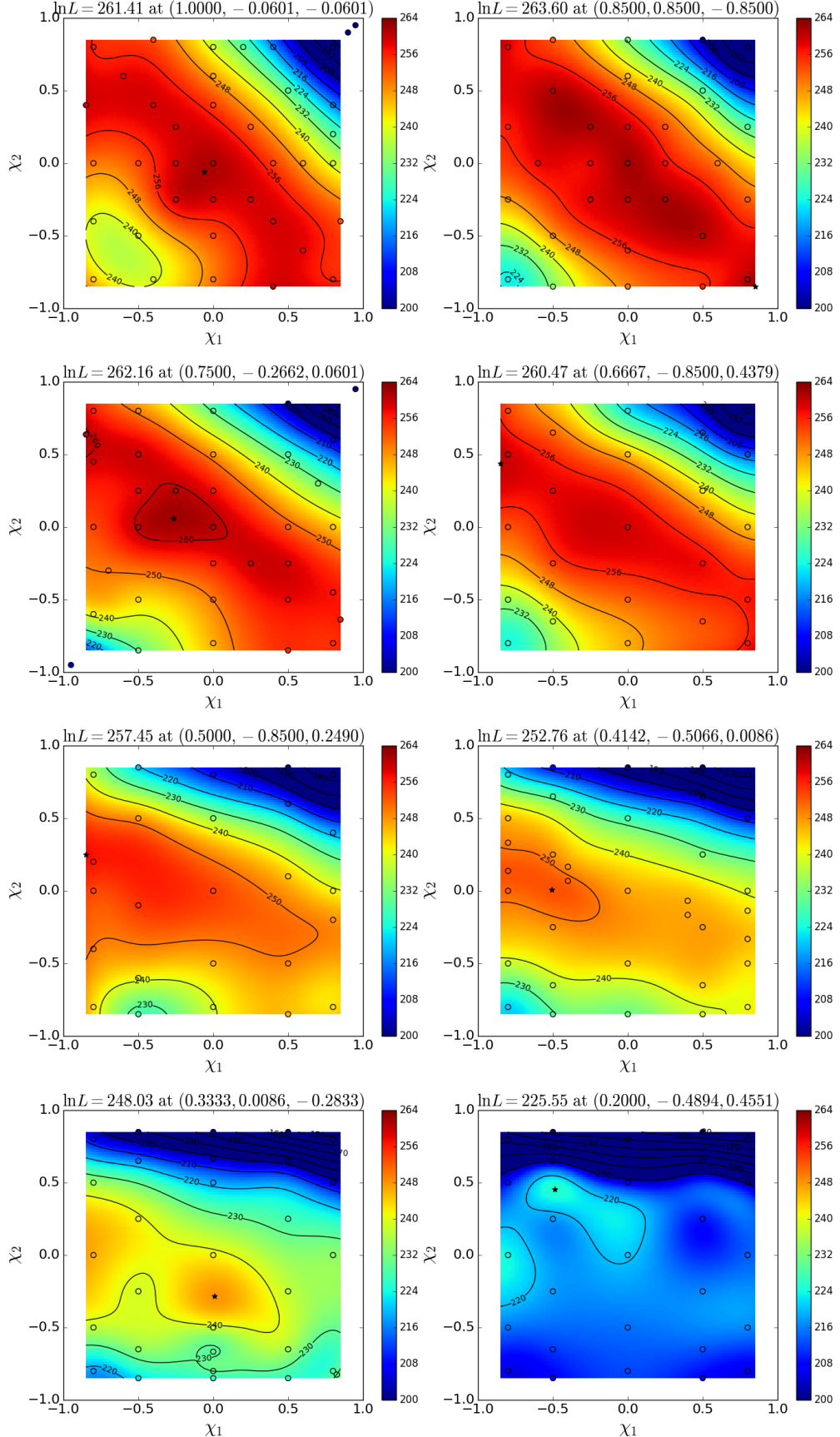


FIG. 4. Heat maps of the GW150914 likelihood for each of the eight mass ratio panels covering form $q = 1$ to $q = 1/5$ and aligned/antialigned individual spins. The individual panel with $q = 0.85$ contains the highest likelihood. Contour lines are in increments of 5. The interpolated $\ln \mathcal{L}$ maximum at its location in (q, χ_1, χ_2) space is given in each panel's title and denoted by the * in the plots.

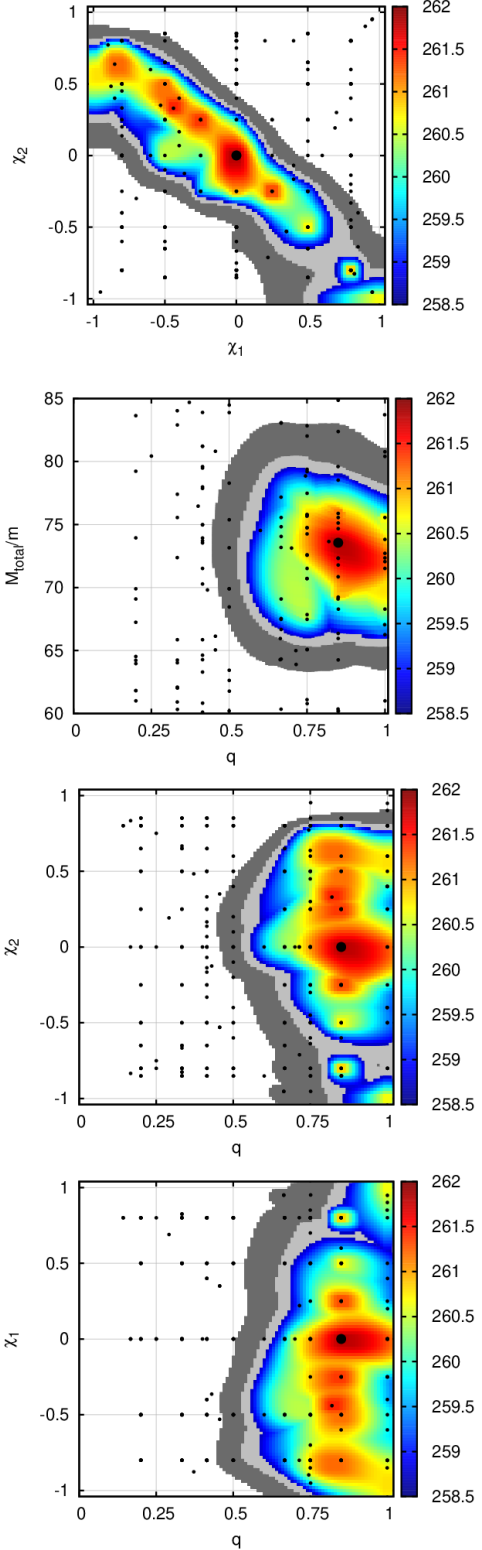


FIG. 5. 90% confidence interval heat maps of the GW150914 likelihood for the aligned binary mass ratio and individual spin parameters. The dark grey region constitutes the 99.7% (3σ) confidence interval range, and the light grey is the 95% (2σ) range. The colored region shows the $\ln \mathcal{L}$ of the values within the 90% confidence interval. The black points indicate the placement of the numerical simulations.

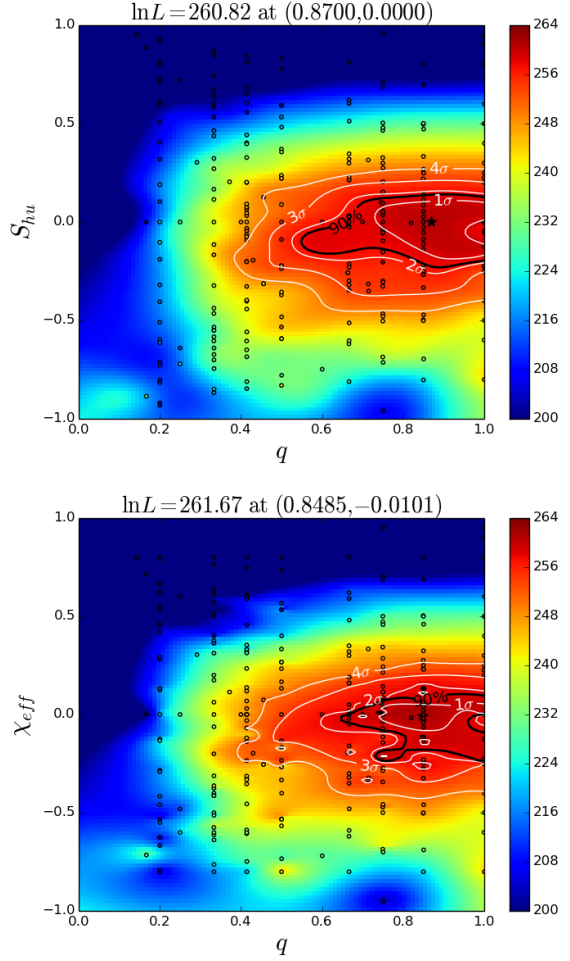


FIG. 6. Heat maps of the GW150914 likelihood for the aligned binary with effective variables S_{hu} and χ_{eff} versus mass ratios using linear interpolation. In black the 90% confidence contours and the interpolated $\ln \mathcal{L}$ maximum is given in each panel's title and denoted by the * in the plots.

The latter exhibits some “pinch” points around some simulations suggesting a remaining degeneracy by using χ_{eff} . Such features are not seen using the (normalized) variable S_{hu} , which represents a better fitting to waveform phases as shown in [30], suggesting again that it is a better (or at least a valid alternative) choice to describe aligned binaries.

The 3D interpolated results give a maximum $\ln \mathcal{L}$ of 261.8 at $(M_{total}, q, \chi_1, \chi_2) = (73.6, 0.8500, 0.0000, 0.0000)$. Values of the final mass and spin for this point are 0.952 and 0.683, respectively, and the recoil velocity is 44 km/s. The mean values from the GW150914 properties paper [4] are 0.955 and 0.67 for the final mass and spin, respectively. Converting the final mass to energy radiated and calculating the ranges in these final parameters from the simulations that fall within the 90% confidence interval as shown in Fig. 7,

we find

$$\begin{aligned} 0.039 < E_{rad}/m < 0.053 \\ 0.578 < \chi_f < 0.753 \\ 0 < V_{recoil} < 492[\text{km/s}] \end{aligned}$$

Comparing these ranges to the GW150914 properties paper [4] (and converting from total mass and final mass to energy radiated and propagating the errors appropriately)

$$\begin{aligned} 0.041 < E_{rad}/m < 0.049 \\ 0.60 < \chi_f < 0.72 \end{aligned}$$

Note that a final recoil velocity is not estimated in [4].

B. Precessing binaries

An analogous study of GW150914 using the aligned spin binaries above can be done in a completely independent way with a set of precessing binaries. We supplement the new simulations in this catalog release with those reported in Ref. [92, 98] for mass-ratio families of binaries with one spinning black hole pointing along 32 different orientations. The results of evaluation of the $\ln \mathcal{L}$ for a set of six different mass ratio families are displayed in Fig. 8. We find that the highest likelihood, is displayed in the $q = 1$ panel and spin orientation near the equatorial (orbital) plane. This result is consistent with the low S_{hu} (or low χ_{eff}) displayed in Fig. 6. The $q = 1$ highest likelihood is bracketed by the $q = 1.4$ and $q = 0.66$ panels with the former having a larger $\ln \mathcal{L}$ than the later, indicating that the optimal configuration should have a mass ratio between $q = 1$ and $q = 1.40$ (that corresponds to a case of $q = 1/1.4 = 0.714$ with the smaller black hole spinning). This again is in agreement with the previous analysis involving only aligned simulations indicating a preference for mass ratios around $q = 0.85$.

Let us note that this precessing simulations analysis is completely independent from the previous nonprecessing, aligned spins, and they do not share simulations in common and yet lead to a similar range of parameters (for the most robust mass ratios and projections of the spins onto the orbital angular momentum). While the analysis would benefit from more simulations to populate this 4D parameter space (and this will be one of the subjects of a new catalog release), it is encouraging that consistent results are already found with this minimal set of nearly 200 simulations. we populated each panel with 4 sets of initial $\theta = 30, 60, 90, 135$ degrees orientations (note that new configurations will supplant $\theta = 135$ for 120 and 150 degrees) and six $\phi = 0, 30, 60, 90, 120, 150$ plus the poles and a few control simulations on the $\phi < 0$ degrees (See Fig. 7 of Ref. [87]). To extrapolate into the western hemisphere, we exploit the symmetry of the parameter space and fit a sinusoidal function to the available numerical

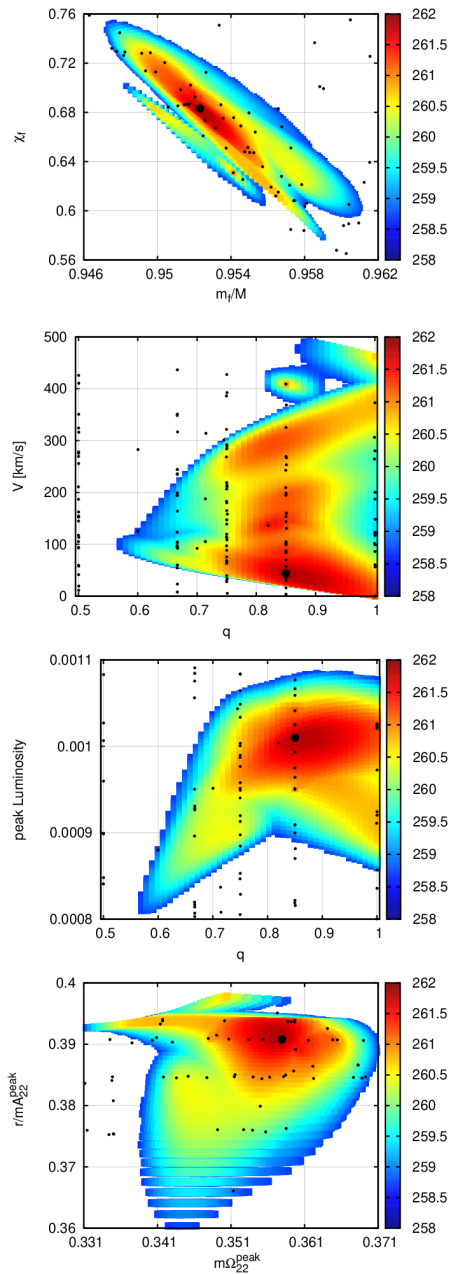


FIG. 7. Final parameter space heatmaps for simulations that fall within the 90% confidence interval for the final mass, spin, recoil, peak luminosity, and orbital frequency and strain amplitude at peak strain. A maximum $\ln \mathcal{L}$ is reached for $m_f/m = 0.952$, $\chi_f = 0.683$, $V = 44 \text{ km/s}$, $L^{peak} = 1.01e-3$, $m\Omega_{22}^{peak} = 0.358$, and $(r/m)A_{22}^{peak} = 0.391$.

simulations. Instead of plotting in the angles θ and ϕ , we plot in the Hammer-Aitoff coordinates [99], which is a coordinate system where the whole angular space can be viewed as a 2D map. The points at the top left and bottom left are the poles, $\theta = 0$ at the top, and $\theta = \pi$ at the bottom. The line connecting the two is the $\phi = 0$ line. As you move from left to right from the center, ϕ

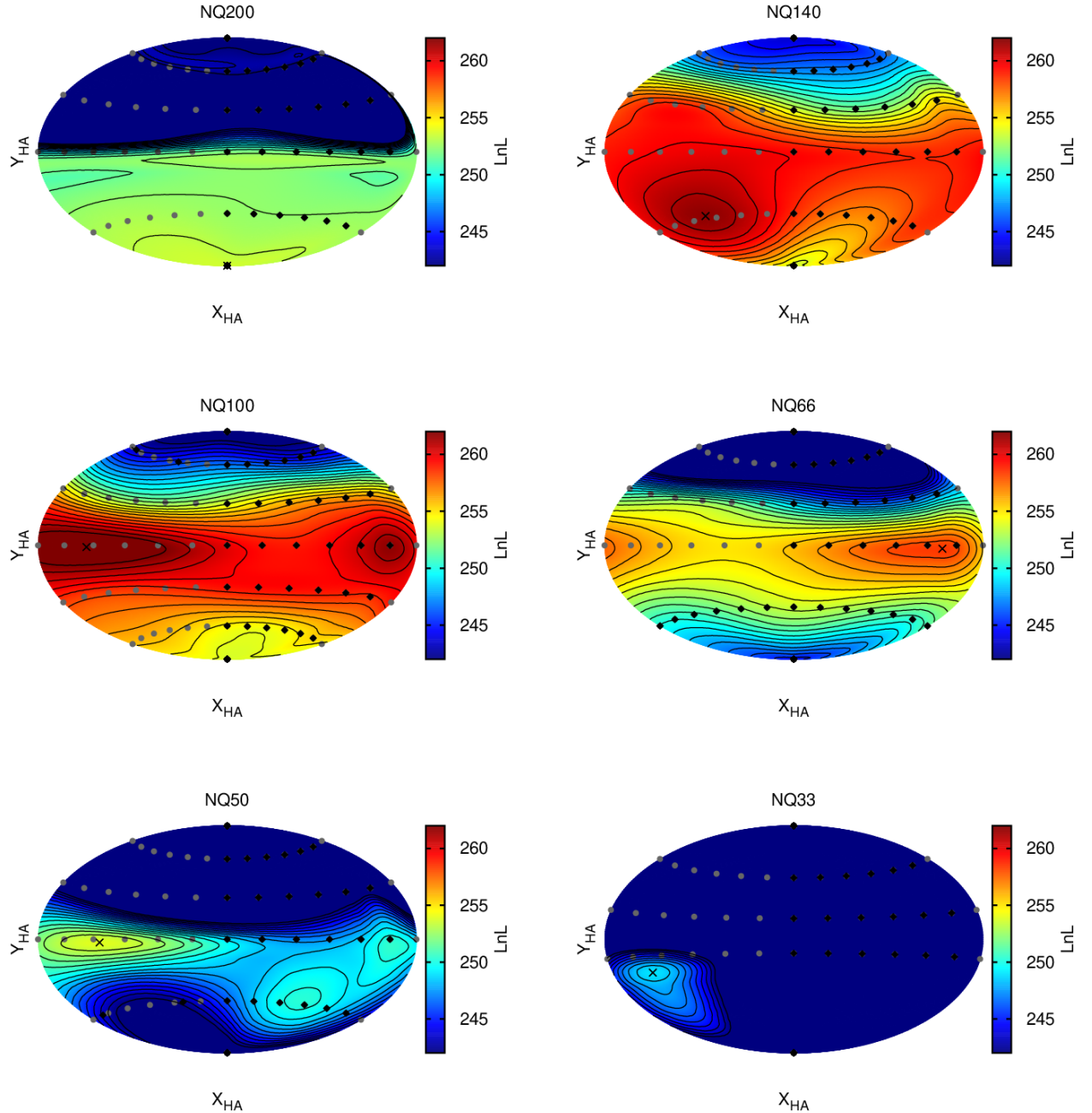


FIG. 8. Heat maps of the GW150914 likelihood for each of the six mass ratio panels covering form $q = 2$ to $q = 1/3$ (labeled from NQ200 to NQ33 respectively) and large black hole spin oriented over the sphere (interpolated using multiquadric radial basis functions between simulations). The individual panel with $q = 1$ contains the highest likelihood (near the orbital plane orientation), and it is bracketed by the $q = 1.4$ and $q = 0.66$ panels ($q > 1$ here means the smaller black hole is the one spinning). We have used Hammer-Aitoff coordinates X_{HA}, Y_{HA} , to represent the map and level curves. The interpolated $\ln \mathcal{L}$ maximum location is denoted by the an x in the plots, the black points are simulations, and the gray points are extrapolated simulations using the sinusoidal dependence of the azimuthal angle.

increases from 0 to 180 degrees, and from right to left, ϕ decreases from 0 to -180 degrees.

C. Estimation of extrinsic parameters

To complete the parameter determination from only the numerical relativity simulations we proceed to compute the distribution of the sky location, distance and binary orientation from the evaluations of the $\ln \mathcal{L}$ for each of our simulations on a total mass grid of 100 points between 40 and 120 M_{\odot} . The results for GW150914 are displayed in Fig. 9. The gray boundaries are calculated from the LIGO GWTC-1 public data [100] for GW150914 by first constructing a 2D kernel destiny estimation and using numpy's percentile function. Simulations within a $\ln \mathcal{L}$ cut of 3.125 of the max are included in the 90% CI interval. As with the intrinsic parameters, the results are consistent but less confined than the LIGO results. Our results seem also to be compatible with the original localization in sky estimates displayed in Ref. [101]

D. Simulated versus signal waveform comparison

We use standard techniques [9, 59] to directly compare GW150914 to our simulations. For each simulation, direct comparison of our simulations to the data selects a fiducial total mass which best fits the observations, as measured by the marginalized likelihood. We can for each simulation select the binary extrinsic parameters like event time and sky location which maximize the likelihood of the data, given our simulation and mass. Then, using these extrinsic parameters, we evaluate the expected detector response in the LIGO Hanford (H1) and Livingston (L1) instruments. Figure 10 displays these reconstructions for the highest log-likelihood NR waveform of the nonprecessing and precessing simulations labeled as RIT:BBH:0113 and RIT:BBH:0126 in our catalog. The details of these simulations are provided in Table I. They directly compare to the signals as observed by LIGO H1 and L1 and with each other. The lower panel shows the residuals of the signals with respect to the RIT simulations. A similar analysis was performed in Ref. [87], Figures 4-6, for the GW170104 event.

V. CONCLUSIONS AND DISCUSSION

The breakthroughs [1–3] in numerical relativity were instrumental in identifying the first detection of gravitational waves [4] with the merger of two black holes. We have shown in this paper that the use of numerical relativity waveform catalogs provides a consistent method for parameter estimation from the observed gravitational waves from merging binary black holes (See also Refs. [9, 59, 102]. It is worthwhile stressing here that

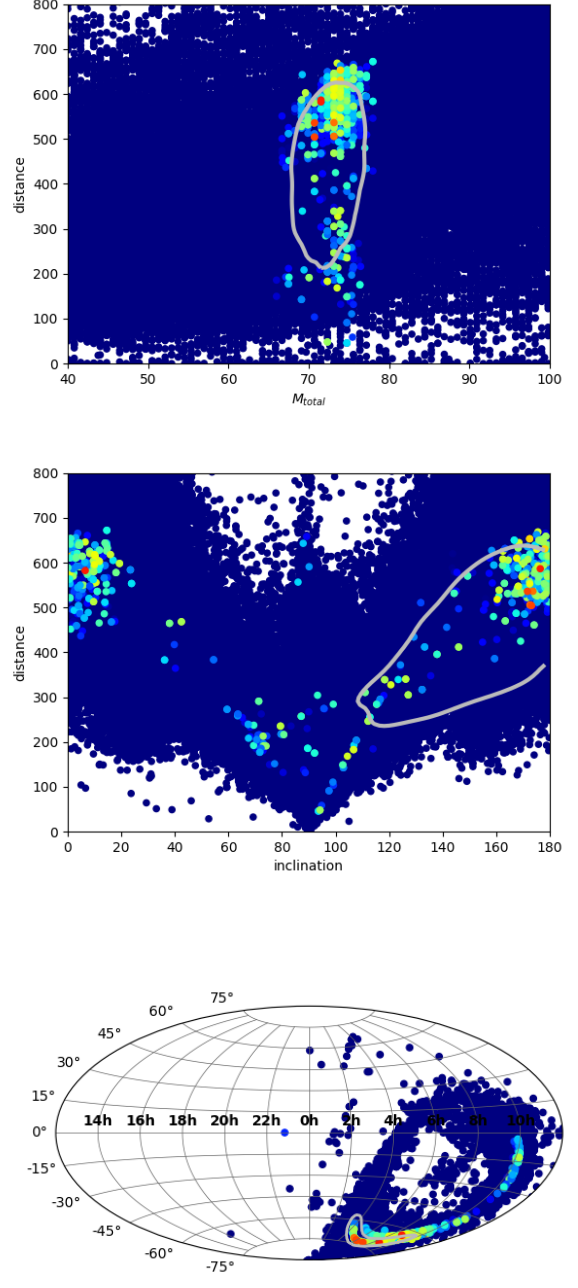


FIG. 9. We use the results of the Monte-Carlo intrinsic log-likelihood calculations (100 samples in M_{total} for each simulation in the catalog) to estimate the extrinsic parameters of GW150914. The gray boundary denotes the public LIGO GWTC-1 data and the colored points indicate simulations which fell within the $\ln \mathcal{L} > \max \ln \mathcal{L} - 3.125$, or roughly the 90% confidence interval. The dark blue background points denote simulations outside of the 90% confidence interval.

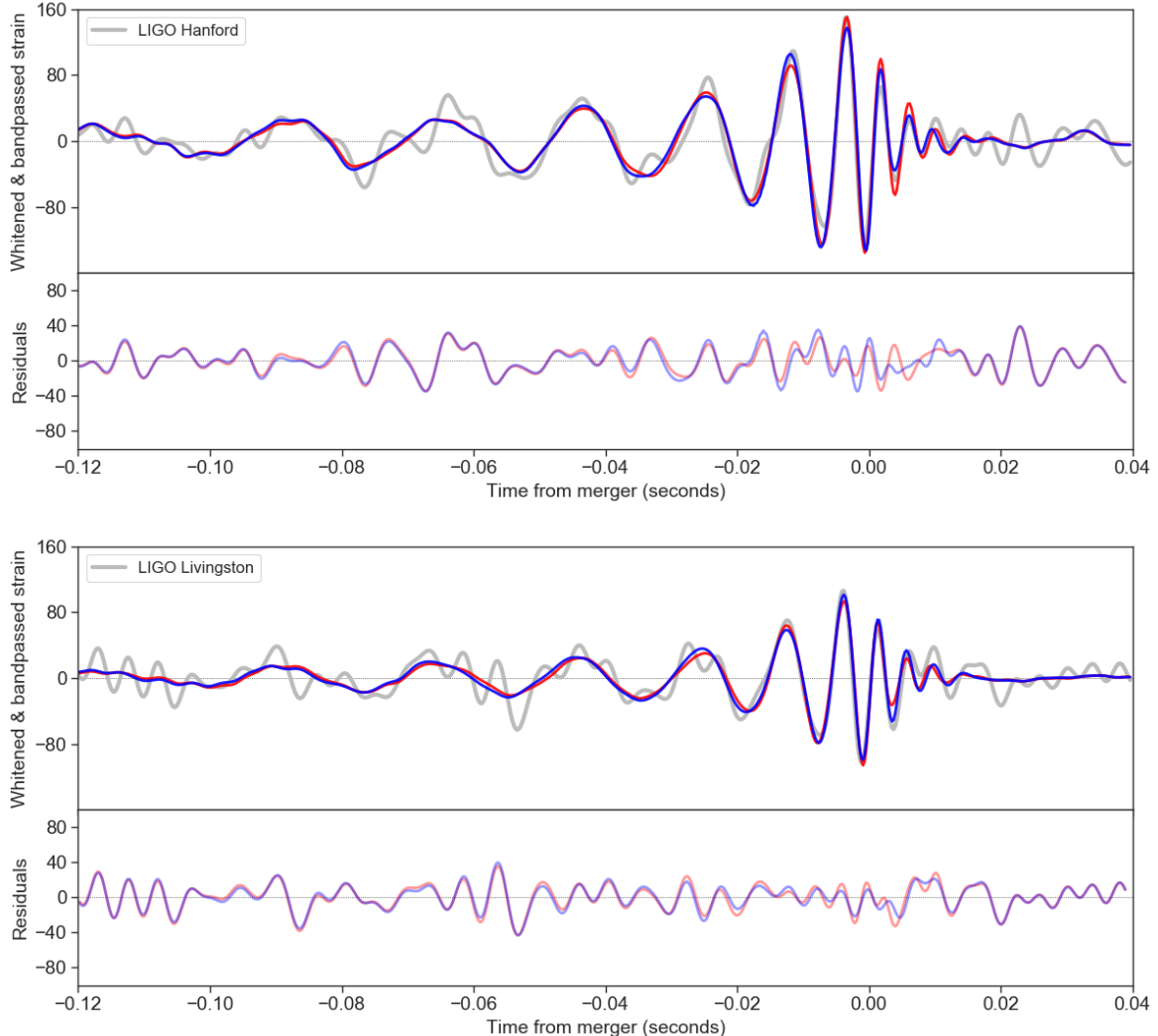


FIG. 10. Direct comparison of the highest $\ln \mathcal{L}$ nonprecessing simulation (RIT:BBH:0113 in red) and precessing simulation (RIT:BBH:0126 in blue) to the Hanford (top) and Livingston (bottom) GW150914 signals. The bottom panel in each figure shows the residual between the whitened NR waveform and detector signal.

TABLE I. Highest $\ln \mathcal{L}$ nonprecessing and precessing simulations. The nonprecessing simulation has highest overall $\ln \mathcal{L}$, and the precessing simulation has 13th highest.

Config.	q	$\vec{\chi}_1$	$\vec{\chi}_2$	\vec{S}_{hu}/m^2	M_{total}/M_\odot	$\ln \mathcal{L}$
RIT:BBH:0113	0.85	(0, 0, 0)	(0, 0, 0)	(0, 0, 0)	73.6	261.8
RIT:BBH:0126	0.75	(-0.46, -0.48, -0.44)	(0.06, -0.38, 0.12)	(-0.15, -0.42, -0.11)	72.5	260.5

this current method of direct comparison of the gravitational wave signal with numerical waveforms does not rely *at all* on any information from the phenomenological models [103, 104] (Phenom or SEOBNR). It also shows that with the current aligned spin coverage one can successfully carry out parameter estimations with results, at least as good as with the phenomenological models [4]; see Lange et al (in prep). We also note that any new simulation produced (for instance targeted to followup

any new detection or catalog expansions) will contribute to improve the binary parameter coverage, thus reducing the interpolation error. The next step will be reduce the extrapolation error at very high spins by adding more simulations with spin magnitudes above 0.90. Also the extension of the family of simulations displayed in Fig. 8 to smaller mass ratios, i.e. $q < 1/3$. Coverage for low total binary masses (below $20M_\odot$), in turn, would require longer full numerical simulations or hybridization of the

current NR waveforms with post-Newtonian waveforms.

The next area of development for the numerical relativity waveform catalogs is the coverage of precessing binaries. Those require expansions of the parameter space to seven dimensions (assuming negligible eccentricity), and is being carried out in a hierarchical approach by neglecting the effects of the spin of the secondary black holes, which is a good assumption for small mass ratios. This approach has proven also successful when applied to GW170104 [87]. It required an homogeneous set of simulations since the differences in $\ln \mathcal{L}$ are subtle. The comparison of different approaches to solve the binary black hole problem has produced an excellent agreement for the GW150914 [11] and GW170104 [87], including higher (up to $\ell = 5$) modes. This leads to the possibility of regularly using multiple catalogs of numerical relativity waveforms to further improve parameter coverage as started in [9]. In a follow up paper we plan to use this upgraded catalog to evaluate the parameters of the ten binary black hole mergers reported recently by LIGO-Virgo O1-O2 observing runs[105].

Aside from the interest in producing waveforms for direct comparison with observation, the simulations of orbiting black-hole binaries produce information about the final remnant of the merger of the two holes. Numerous empirical formulas relating the initial parameters ($q, \vec{\chi}_1, \vec{\chi}_2$) (individual masses and spins) of the binary to those of the final remnant ($m_f, \vec{\chi}_f, \vec{V}_f$) have been proposed. These include formulas for the final mass, spin, and recoil velocity [29, 84, 92, 106–111], the computation of the peak frequency of the (2,2) mode Ω_{22}^{peak} , peak waveform amplitude A_{22}^{peak} [30, 85] and peak luminosity [4, 7, 68, 112]. Those formulas in turn provide further tools to extract information from the observation of gravitational waves, see for instance our Fig. 7.

TABLE II: Initial data parameters for the quasi-circular configurations with a smaller mass black hole (labeled 1), and a larger mass spinning black hole (labeled 2). The punctures are located at $\vec{r}_1 = (x_1, 0, 0)$ and $\vec{r}_2 = (x_2, 0, 0)$, with individual linear momenta $P = \pm(P_r, P_t, 0)$, spin magnitudes $|S_i|$, puncture mass parameters m^p/m , horizon (Christodoulou) masses m^H/m , total ADM mass M_{ADM} , and dimensionless spins $|a/m_H| = |S/m_H^2|$. The spin directions for the precessing simulations are given in the catalog and in Tab. IV.

Run	x_1/m	x_2/m	P_r/m	P_t/m	m_1^p/m	m_2^p/m	$ S_1/m^2 $	$ S_2/m^2 $	m_1^H/m	m_2^H/m	M_{ADM}/m	$ a_1/m_1^H $	$ a_2/m_2^H $
RIT:BBH:0127	-5.71	4.29	0	0.09386	0.2578	0.347	0.1469	0.2612	0.4286	0.5714	0.9901	0.8	0.8
RIT:BBH:0128	-6.67	3.33	0	0.08542	0.1992	0.4072	0.08889	0.3556	0.3333	0.6667	0.9911	0.8	0.8
RIT:BBH:0129	-7.50	2.50	0	0.07226	0.1485	0.4604	0.05	0.45	0.25	0.75	0.9925	0.8	0.8
RIT:BBH:0130	-5.71	4.29	0	0.09362	0.2578	0.3469	0.1469	0.2612	0.4286	0.5714	0.9901	0.8	0.8
RIT:BBH:0131	-6.67	3.33	0	0.08502	0.1992	0.4072	0.08889	0.3556	0.3333	0.6667	0.9911	0.8	0.8
RIT:BBH:0132	-7.50	2.50	0	0.07189	0.1485	0.4603	0.05	0.45	0.25	0.75	0.9925	0.8	0.8
RIT:BBH:0136	-10.00	5.00	0	0.06464	0.3248	0.546	0	0.2667	0.3333	0.6667	0.9934	0	0.6
RIT:BBH:0220	-7.50	5.00	-4.96e-04	0.08177	0.3889	0.3666	0	0.288	0.4	0.6	0.9921	0	0.8
RIT:BBH:0221	-10.83	2.17	-1.51e-04	0.04638	0.09955	0.7352	0.02222	0.3472	0.1667	0.8333	0.9957	0.8	0.5

Continued on next page

ACKNOWLEDGMENTS

The authors thank A. Williamson for assistance with Fig. 10. The authors also gratefully acknowledge the National Science Foundation (NSF) for financial support from Grants No. PHY-1607520, No. PHY-1707946, No. ACI-1550436, No. AST-1516150, No. ACI-1516125, No. PHY-1726215. This work used the Extreme Science and Engineering Discovery Environment (XSEDE) [allocation TG-PHY060027N], which is supported by NSF grant No. ACI-1548562. Computational resources were also provided by the NewHorizons, BlueSky Clusters, and Green Prairies at the Rochester Institute of Technology, which were supported by NSF grants No. PHY-0722703, No. DMS-0820923, No. AST-1028087, No. PHY-1229173, and No. PHY-1726215.

Appendix A: Tables of initial data and results of the new simulations

In this appendix we provide tables with the relevant BBH configuration details. In Table II, we provide the initial data parameters used to start the full numerical evolutions. In Tables III and IV, we provide the binary mass and spin parameters after they settle into a more physical value after radiating and absorbing the spurious gravitation wave content from the initial mathematical choice of conformal flatness. These relaxed values are calculated at a fiducial $t = 200M$.

In Table V we provide the initial orbital frequency and eccentricity, as well as the number of orbits to merger and the final eccentricity. The eccentricity is expected to be reduced from its initial value by gravitational radiation, at a rate proportional to $d^{19/12}$ according to [113], with d , the separation of the binary (see, for instance, Fig. 6 of Ref. [114] or Fig. 9 in Ref. [14]).

Finally, In Table VI, we provide the values of the energy radiated during the simulation and the final black hole spin as measured through the (most accurate) isolated horizon formalism [74].

TABLE II – continued from previous page

Run	x_1/m	x_2/m	P_r/m	P_t/m	m_1^p/m	m_2^p/m	$ S_1/m^2 $	$ S_2/m^2 $	m_1^H/m	m_2^H/m	M_{ADM}/m	$ a_1/m_1^H $	$ a_2/m_2^H $
RIT:BBH:0222	-10.83	2.17	-1.20e-04	0.04418	0.09964	0.7352	0.02222	0.3472	0.1667	0.8333	0.9954	0.8	0.5
RIT:BBH:0223	-7.03	5.97	-4.30e-04	0.08115	0.279	0.5162	0.1689	0.07305	0.4595	0.5405	0.992	0.8	0.25
RIT:BBH:0224	-10.83	2.17	-1.09e-04	0.04312	0.09967	0.515	0.02222	0.5556	0.1667	0.8333	0.9954	0.8	0.8
RIT:BBH:0226	-10.83	2.17	-1.27e-04	0.0447	0.09961	0.8278	0.02222	0	0.1667	0.8333	0.9955	0.8	0
RIT:BBH:0227	-7.03	5.97	-3.89e-04	0.07931	0.279	0.5163	0.1689	0.07305	0.4595	0.5405	0.9918	0.8	0.25
RIT:BBH:0228	-6.50	6.50	-3.94e-04	0.07983	0.2579	0.4557	0.2125	0.1	0.5	0.5	0.9918	0.85	0.4
RIT:BBH:0230	-7.50	5.00	-4.73e-04	0.08102	0.3889	0.3666	0	0.288	0.4	0.6	0.992	0	0.8
RIT:BBH:0231	-7.50	5.00	-4.74e-04	0.08104	0.3889	0.3666	0	0.288	0.4	0.6	0.992	0	0.8
RIT:BBH:0232	-7.03	5.97	-5.02e-04	0.08372	0.2789	0.3295	0.1689	0.2337	0.4595	0.5405	0.9924	0.8	0.8
RIT:BBH:0233	-7.50	5.00	-4.76e-04	0.08111	0.3889	0.3666	0	0.288	0.4	0.6	0.9921	0	0.8
RIT:BBH:0234	-7.50	5.00	-4.77e-04	0.08113	0.3889	0.3666	0	0.288	0.4	0.6	0.9921	0	0.8
RIT:BBH:0235	-7.50	5.00	-4.76e-04	0.08111	0.3889	0.3666	0	0.288	0.4	0.6	0.9921	0	0.8
RIT:BBH:0236	-7.50	5.00	-4.74e-04	0.08104	0.3889	0.3666	0	0.288	0.4	0.6	0.992	0	0.8
RIT:BBH:0237	-6.86	5.14	-5.90e-04	0.08569	0.311	0.5391	0.1286	0.09796	0.4286	0.5714	0.9917	0.7	0.3
RIT:BBH:0238	-6.86	5.14	-6.35e-04	0.08695	0.3701	0.2953	0.09184	0.2776	0.4286	0.5714	0.9919	0.5	0.85
RIT:BBH:0239	-6.86	5.14	-5.61e-04	0.08478	0.3702	0.2953	0.09184	0.2776	0.4286	0.5714	0.9916	0.5	0.85
RIT:BBH:0240	-7.03	5.97	-4.87e-04	0.08322	0.3983	0.2793	0.1056	0.2484	0.4595	0.5405	0.9922	0.5	0.85
RIT:BBH:0241	-5.62	4.19	-9.95e-04	0.09488	0.1605	0.3708	0.1634	0.2534	0.4271	0.5729	0.9901	0.8957	0.7719
RIT:BBH:0242	-7.50	5.00	-4.74e-04	0.08104	0.3889	0.3666	0	0.288	0.4	0.6	0.992	0	0.8
RIT:BBH:0243	-7.50	5.00	-4.76e-04	0.08111	0.3889	0.3666	0	0.288	0.4	0.6	0.9921	0	0.8
RIT:BBH:0244	-7.50	5.00	-4.74e-04	0.08104	0.3889	0.3666	0	0.288	0.4	0.6	0.992	0	0.8
RIT:BBH:0245	-8.67	4.33	-3.67e-04	0.07335	0.2871	0.3467	0.05556	0.3778	0.3333	0.6667	0.9929	0.5	0.85
RIT:BBH:0246	-10.83	2.17	-1.34e-04	0.04524	0.0996	0.8277	0.02222	0	0.1667	0.8333	0.9955	0.8	0
RIT:BBH:0247	-8.67	4.33	-2.97e-04	0.07024	0.2873	0.3467	0.05556	0.3778	0.3333	0.6667	0.9926	0.5	0.85
RIT:BBH:0248	-7.50	5.00	-4.73e-04	0.08102	0.3889	0.3666	0	0.288	0.4	0.6	0.992	0	0.8
RIT:BBH:0249	-7.03	5.97	-3.85e-04	0.07913	0.3718	0.5299	0.1267	0	0.4595	0.5405	0.9917	0.6	0
RIT:BBH:0250	-7.50	5.00	-4.77e-04	0.08113	0.3889	0.3666	0	0.288	0.4	0.6	0.9921	0	0.8
RIT:BBH:0251	-7.50	5.00	-4.76e-04	0.08111	0.3889	0.3666	0	0.288	0.4	0.6	0.9921	0	0.8
RIT:BBH:0252	-6.86	5.14	-4.43e-04	0.08022	0.3704	0.2954	0.09184	0.2776	0.4286	0.5714	0.9912	0.5	0.85
RIT:BBH:0253	-4.00	4.00	0	0.104	0.5	0.5	0.2375	0.2375	0.5156	0.5156	0.9883	0.95	0.95
RIT:BBH:0254	-7.03	5.97	-4.35e-04	0.08135	0.3718	0.5298	0.1267	0	0.4595	0.5405	0.9919	0.6	0
RIT:BBH:0255	-6.69	4.46	-5.65e-04	0.08352	0.3878	0.3659	0	0.288	0.4	0.6	0.9908	0	0.8
RIT:BBH:0256	-6.69	4.46	-5.66e-04	0.08354	0.3878	0.3659	0	0.288	0.4	0.6	0.9909	0	0.8
RIT:BBH:0257	-6.69	4.46	-5.67e-04	0.08357	0.3878	0.3658	0	0.288	0.4	0.6	0.9909	0	0.8
RIT:BBH:0258	-6.69	4.46	-5.68e-04	0.08359	0.3878	0.3658	0	0.288	0.4	0.6	0.9909	0	0.8
RIT:BBH:0259	-6.69	4.46	-5.67e-04	0.08357	0.3878	0.3658	0	0.288	0.4	0.6	0.9909	0	0.8
RIT:BBH:0260	-6.69	4.46	-5.66e-04	0.08354	0.3878	0.3659	0	0.288	0.4	0.6	0.9909	0	0.8
RIT:BBH:0261	-6.50	6.50	-4.36e-04	0.08168	0.2579	0.4556	0.2125	0.1	0.5	0.5	0.992	0.85	0.4
RIT:BBH:0262	-6.86	5.14	-4.64e-04	0.08124	0.3111	0.5392	0.1286	0.09796	0.4286	0.5714	0.9912	0.7	0.3
RIT:BBH:0263	-7.03	5.97	-3.56e-04	0.07755	0.3985	0.2794	0.1056	0.2484	0.4595	0.5405	0.9917	0.5	0.85
RIT:BBH:0264	-7.05	4.70	-5.25e-04	0.08267	0.3883	0.3662	0	0.288	0.4	0.6	0.9914	0	0.8
RIT:BBH:0265	-7.03	5.97	-4.32e-04	0.08121	0.3983	0.2794	0.1056	0.2484	0.4595	0.5405	0.992	0.5	0.85
RIT:BBH:0266	-7.05	4.70	-5.28e-04	0.08274	0.3883	0.3662	0	0.288	0.4	0.6	0.9915	0	0.8
RIT:BBH:0267	-7.05	4.70	-5.33e-04	0.08287	0.3883	0.3661	0	0.288	0.4	0.6	0.9915	0	0.8
RIT:BBH:0268	-7.05	4.70	-5.27e-04	0.08274	0.3883	0.3662	0	0.288	0.4	0.6	0.9915	0	0.8
RIT:BBH:0269	-6.84	4.56	-5.45e-04	0.08314	0.388	0.366	0	0.288	0.4	0.6	0.9911	0	0.8
RIT:BBH:0270	-6.84	4.56	-5.48e-04	0.08319	0.388	0.366	0	0.288	0.4	0.6	0.9911	0	0.8
RIT:BBH:0271	-6.84	4.56	-5.52e-04	0.08329	0.388	0.3659	0	0.288	0.4	0.6	0.9912	0	0.8
RIT:BBH:0272	-6.84	4.56	-5.54e-04	0.08334	0.388	0.3659	0	0.288	0.4	0.6	0.9912	0	0.8
RIT:BBH:0273	-6.84	4.56	-5.52e-04	0.08329	0.388	0.3659	0	0.288	0.4	0.6	0.9912	0	0.8
RIT:BBH:0274	-6.84	4.56	-5.47e-04	0.08319	0.388	0.366	0	0.288	0.4	0.6	0.9911	0	0.8
RIT:BBH:0276	-7.03	5.97	-4.62e-04	0.08235	0.279	0.5162	0.1689	0.07305	0.4595	0.5405	0.9921	0.8	0.25
RIT:BBH:0277	-7.03	5.97	-3.87e-04	0.07925	0.3985	0.2794	0.1056	0.2484	0.4595	0.5405	0.9918	0.5	0.85
RIT:BBH:0278	-10.83	2.17	-1.15e-04	0.04369	0.09965	0.7352	0.02222	0.3472	0.1667	0.8333	0.9954	0.8	0.5
RIT:BBH:0279	-7.03	5.97	-4.62e-04	0.08235	0.3983	0.4705	0.1056	0.1461	0.4595	0.5405	0.992	0.5	0.5
RIT:BBH:0280	-7.05	4.70	-5.34e-04	0.08287	0.3883	0.3661	0	0.288	0.4	0.6	0.9915	0	0.8
RIT:BBH:0281	-7.05	4.70	-5.36e-04	0.08293	0.3883	0.3661	0	0.288	0.4	0.6	0.9916	0	0.8
RIT:BBH:0283	-7.20	4.80	-6.30e-04	0.08574	0.2415	0.3663	0.128	0.288	0.4	0.6	0.9922	0.8	0.8
RIT:BBH:0284	-9.00	3.00	-3.91e-04	0.0671	0.2136	0.3911	0.03125	0.4781	0.25	0.75	0.9938	0.5	0.85
RIT:BBH:0285	-8.25	2.75	-3.49e-04	0.06534	0.2132	0.3908	0.03125	0.4781	0.25	0.75	0.9928	0.5	0.85
RIT:BBH:0286	-9.00	3.00	-3.64e-04	0.06616	0.2137	0.3912	0.03125	0.4781	0.25	0.75	0.9937	0.5	0.85

Continued on next page

TABLE II – continued from previous page

Run	x_1/m	x_2/m	P_r/m	P_t/m	m_1^p/m	m_2^p/m	$ S_1/m^2 $	$ S_2/m^2 $	m_1^H/m	m_2^H/m	M_{ADM}/m	$ a_1/m_1^H $	$ a_2/m_2^H $
RIT:BBH:0287	-7.20	4.80	-5.25e-04	0.0826	0.2415	0.3664	0.128	0.288	0.4	0.6	0.9918	0.8	0.8
RIT:BBH:0288	-8.25	2.75	-3.35e-04	0.06449	0.2132	0.3908	0.03125	0.4781	0.25	0.75	0.9927	0.5	0.85
RIT:BBH:0289	-7.20	4.80	-4.73e-04	0.08083	0.2416	0.3664	0.128	0.288	0.4	0.6	0.9916	0.8	0.8
RIT:BBH:0290	-5.71	4.29	-1.40e-03	0.1082	0.4286	0.5714	0.1745	0.3102	0.4286	0.5714	0.9894	0.95	0.95
RIT:BBH:0291	-7.20	4.80	-4.34e-04	0.07908	0.3451	0.4661	0.08	0.234	0.4	0.6	0.9913	0.5	0.65
RIT:BBH:0292	-7.20	4.80	-4.18e-04	0.07823	0.2417	0.3664	0.128	0.288	0.4	0.6	0.9914	0.8	0.8
RIT:BBH:0293	-7.20	4.80	-4.71e-04	0.08074	0.3451	0.466	0.08	0.234	0.4	0.6	0.9915	0.5	0.65
RIT:BBH:0294	-7.20	4.80	-5.41e-04	0.08319	0.2416	0.5889	0.128	0	0.4	0.6	0.9918	0.8	0
RIT:BBH:0295	-7.20	4.80	-4.33e-04	0.07899	0.2417	0.5232	0.128	0.18	0.4	0.6	0.9914	0.8	0.5
RIT:BBH:0296	-8.67	4.33	-4.00e-04	0.07477	0.287	0.3466	0.05556	0.3778	0.3333	0.6667	0.9931	0.5	0.85
RIT:BBH:0297	-7.20	4.80	-4.96e-04	0.08169	0.2416	0.5231	0.128	0.18	0.4	0.6	0.9917	0.8	0.5
RIT:BBH:0298	-7.20	4.80	-4.58e-04	0.08014	0.3451	0.5739	0.08	0.09	0.4	0.6	0.9914	0.5	0.25
RIT:BBH:0299	-9.19	3.81	-3.51e-04	0.0698	0.2517	0.3684	0.04289	0.425	0.2929	0.7071	0.9936	0.5	0.85
RIT:BBH:0300	-9.19	3.81	-3.26e-04	0.06877	0.2517	0.3684	0.04289	0.425	0.2929	0.7071	0.9934	0.5	0.85
RIT:BBH:0301	-7.20	4.80	-5.94e-04	0.08476	0.2415	0.523	0.128	0.18	0.4	0.6	0.992	0.8	0.5
RIT:BBH:0302	-7.20	4.80	-5.47e-04	0.08339	0.345	0.5738	0.08	0.09	0.4	0.6	0.9917	0.5	0.25
RIT:BBH:0303	-7.29	5.21	-4.14e-04	0.07919	0.2522	0.5726	0.1389	0	0.4167	0.5833	0.9917	0.8	0
RIT:BBH:0304	-7.20	4.80	-5.28e-04	0.08271	0.3449	0.466	0.08	0.234	0.4	0.6	0.9917	0.5	0.65
RIT:BBH:0305	-7.20	4.80	-5.02e-04	0.08188	0.345	0.5738	0.08	0.09	0.4	0.6	0.9916	0.5	0.25
RIT:BBH:0306	-7.20	4.80	-5.90e-04	0.08465	0.3449	0.4659	0.08	0.234	0.4	0.6	0.9919	0.5	0.65
RIT:BBH:0307	-7.20	4.80	-4.63e-04	0.08032	0.2416	0.589	0.128	0	0.4	0.6	0.9915	0.8	0
RIT:BBH:0308	-7.20	4.80	-4.99e-04	0.08172	0.2416	0.5231	0.128	0.18	0.4	0.6	0.9917	0.8	0.5
RIT:BBH:0309	-7.20	4.80	-4.94e-04	0.08154	0.345	0.5739	0.08	0.09	0.4	0.6	0.9915	0.5	0.25
RIT:BBH:0311	-7.20	4.80	-4.61e-04	0.0803	0.3886	0.5231	0	0.18	0.4	0.6	0.9914	0	0.5
RIT:BBH:0312	-7.20	4.80	-5.42e-04	0.0832	0.3884	0.5231	0	0.18	0.4	0.6	0.9917	0	0.5
RIT:BBH:0314	-8.67	4.33	-2.82e-04	0.06922	0.2873	0.3467	0.05556	0.3778	0.3333	0.6667	0.9925	0.5	0.85
RIT:BBH:0316	-9.19	3.81	-2.55e-04	0.06527	0.2519	0.3684	0.04289	0.425	0.2929	0.7071	0.9931	0.5	0.85
RIT:BBH:0317	-5.71	4.29	-7.48e-04	0.09202	0.4286	0.5714	0.1745	0.3102	0.4286	0.5714	0.988	0.95	0.95
RIT:BBH:0318	-10.83	2.17	-1.64e-04	0.04711	0.1422	0.4366	0.01389	0.5903	0.1667	0.8333	0.9957	0.5	0.85
RIT:BBH:0319	-7.29	5.21	-4.83e-04	0.08199	0.2522	0.5725	0.1389	0	0.4167	0.5833	0.992	0.8	0
RIT:BBH:0321	-10.83	2.17	-1.58e-04	0.04672	0.1422	0.4366	0.01389	0.5903	0.1667	0.8333	0.9957	0.5	0.85
RIT:BBH:0322	-9.19	3.81	-2.45e-04	0.06445	0.2519	0.3684	0.04289	0.425	0.2929	0.7071	0.993	0.5	0.85
RIT:BBH:0324	-5.50	5.50	-5.85e-04	0.08541	0.1802	0.1802	0.225	0.225	0.5	0.5	0.9904	0.9	0.9
RIT:BBH:0336	-8.67	4.33	-3.48e-04	0.07276	0.2011	0.6573	0.08889	0	0.3333	0.6667	0.9929	0.8	0
RIT:BBH:0337	-10.83	2.17	-1.11e-04	0.0434	0.1424	0.4366	0.01389	0.5903	0.1667	0.8333	0.9953	0.5	0.85
RIT:BBH:0338	-8.67	4.33	-3.11e-04	0.07092	0.2011	0.6574	0.08889	0	0.3333	0.6667	0.9927	0.8	0
RIT:BBH:0339	-9.75	3.25	-2.79e-04	0.06278	0.2413	0.4618	0	0.45	0.25	0.75	0.9941	0	0.8
RIT:BBH:0344	-7.81	4.69	-5.07e-04	0.08096	0.3233	0.3241	0.07031	0.332	0.375	0.625	0.9925	0.5	0.85
RIT:BBH:0345	-10.83	2.17	-1.09e-04	0.04311	0.1424	0.4366	0.01389	0.5903	0.1667	0.8333	0.9953	0.5	0.85
RIT:BBH:0348	-7.81	4.69	-4.52e-04	0.0791	0.3641	0.5459	0	0.1953	0.375	0.625	0.9921	0	0.5
RIT:BBH:0350	-7.81	4.69	-4.88e-04	0.08035	0.3233	0.4863	0.07031	0.2539	0.375	0.625	0.9923	0.5	0.65
RIT:BBH:0352	-7.81	4.69	-4.82e-04	0.08013	0.364	0.3241	0	0.332	0.375	0.625	0.9923	0	0.85

TABLE III: The mass and spin of the nonprecessing BHs in Table II after the BHs had time to equilibrate ($t/m = 200$). Also provided are the difference in the masses, $\delta m = (q-1)/(q+1)$, sum of the spins $S/m^2 = (\chi_{2z} + q^2 \chi_{1z})/(q+1)^2$, and spin difference, $\Delta/m^2 = (\chi_{2z} - q\chi_{1z})/(1+q)$.

Run	q^r	m_1^r/m	m_2^r/m	χ_{1z}^r	χ_{2z}^r	δm_r	S_r/m_r^2	Δ_r/m_r^2
RIT:BBH:0136	0.5001	0.3333	0.6666	0.0000	0.4244	-0.3333	0.2829	0.1886
RIT:BBH:0220	0.6670	0.4000	0.5997	0.0000	-0.8008	-0.1998	-0.4801	-0.2880
RIT:BBH:0221	0.2000	0.1666	0.8333	-0.8005	-0.5000	-0.6667	-0.2833	-0.3694
RIT:BBH:0222	0.2000	0.1666	0.8333	-0.8006	0.5000	-0.6667	0.5500	0.3250
RIT:BBH:0223	0.8496	0.4593	0.5405	-0.8008	0.2500	-0.0813	0.5028	-0.0958
RIT:BBH:0224	0.2001	0.1666	0.8329	0.8006	0.8009	-0.6666	0.5334	0.5778
RIT:BBH:0226	0.2000	0.1666	0.8333	0.8006	0.0000	-0.6667	-0.1334	0.0222
RIT:BBH:0227	0.8496	0.4593	0.5405	0.8007	-0.2500	-0.0813	-0.5028	0.0958
RIT:BBH:0228	0.9993	0.4997	0.5000	0.8512	-0.4000	-0.0003	-0.6251	0.1125
RIT:BBH:0232	0.8500	0.4593	0.5403	-0.8007	-0.8008	-0.0811	-0.0649	-0.4027
RIT:BBH:0237	0.7499	0.4285	0.5714	-0.7003	-0.3000	-0.1429	0.1286	-0.2265

Continued on next page

TABLE III – continued from previous page

Run	q^r	m_1^r/m	m_2^r/m	χ_{1z}^r	χ_{2z}^r	δm_r	S_r/m_r^2	Δ_r/m_r^2
RIT:BBH:0238	0.7505	0.4286	0.5710	-0.5000	-0.8512	-0.1425	-0.2717	-0.3694
RIT:BBH:0239	0.7505	0.4286	0.5710	0.5000	-0.8512	-0.1425	-0.7001	-0.1857
RIT:BBH:0240	0.8506	0.4595	0.5402	-0.5000	-0.8508	-0.0807	-0.2297	-0.3538
RIT:BBH:0241	0.7450	0.4267	0.5728	-0.8972	0.7723	-0.1461	0.8248	0.0900
RIT:BBH:0245	0.5004	0.3333	0.6662	0.5000	-0.8514	-0.3330	-0.7335	-0.3223
RIT:BBH:0246	0.2000	0.1666	0.8333	-0.8004	0.0000	-0.6667	0.1334	-0.0222
RIT:BBH:0247	0.5004	0.3333	0.6662	-0.5000	0.8513	-0.3330	0.7334	0.3222
RIT:BBH:0249	0.8499	0.4594	0.5405	0.6001	0.0000	-0.0811	-0.2757	0.1267
RIT:BBH:0252	0.7505	0.4286	0.5710	0.5000	0.8512	-0.1425	0.2717	0.3694
RIT:BBH:0253	1.0000	0.5010	0.5010	0.9485	0.9485	0.0000	0.0000	0.4761
RIT:BBH:0254	0.8499	0.4594	0.5405	-0.6001	0.0000	-0.0811	0.2757	-0.1267
RIT:BBH:0261	0.9993	0.4997	0.5000	-0.8512	0.4000	-0.0003	0.6251	-0.1125
RIT:BBH:0262	0.7499	0.4285	0.5714	0.7003	0.3000	-0.1429	-0.1286	0.2265
RIT:BBH:0263	0.8506	0.4595	0.5401	0.5000	0.8505	-0.0807	0.2296	0.3537
RIT:BBH:0265	0.8506	0.4595	0.5402	0.5000	-0.8507	-0.0807	-0.6890	-0.1427
RIT:BBH:0276	0.8496	0.4593	0.5405	-0.8008	-0.2500	-0.0813	0.2326	-0.2419
RIT:BBH:0277	0.8506	0.4595	0.5401	-0.5000	0.8506	-0.0807	0.6889	0.1426
RIT:BBH:0278	0.2000	0.1666	0.8333	0.8006	0.5001	-0.6667	0.2833	0.3694
RIT:BBH:0279	0.8500	0.4595	0.5405	-0.5001	-0.5001	-0.0811	-0.0406	-0.2517
RIT:BBH:0283	0.6667	0.3999	0.5997	-0.8007	-0.8006	-0.2000	-0.1599	-0.4160
RIT:BBH:0284	0.3336	0.2500	0.7494	-0.5001	-0.8513	-0.4997	-0.5127	-0.5094
RIT:BBH:0285	0.3336	0.2500	0.7494	-0.5001	0.8513	-0.4997	0.7626	0.4469
RIT:BBH:0286	0.3336	0.2500	0.7494	0.5000	-0.8513	-0.4997	-0.7626	-0.4469
RIT:BBH:0287	0.6667	0.3998	0.5997	0.8007	-0.8008	-0.2000	-0.8001	-0.1600
RIT:BBH:0288	0.3336	0.2500	0.7494	0.5001	0.8513	-0.4997	0.5127	0.5094
RIT:BBH:0289	0.6667	0.3998	0.5997	-0.8007	0.8008	-0.2000	0.8000	0.1600
RIT:BBH:0290	0.7509	0.4282	0.5703	-0.9510	-0.9531	-0.1422	-0.1361	-0.4844
RIT:BBH:0291	0.6668	0.4000	0.5999	0.5001	0.6503	-0.1999	0.1901	0.3140
RIT:BBH:0292	0.6667	0.3998	0.5997	0.8007	0.8007	-0.2000	0.1600	0.4160
RIT:BBH:0293	0.6668	0.4000	0.5999	-0.5001	0.6503	-0.1999	0.5901	0.1540
RIT:BBH:0294	0.6664	0.3998	0.6000	-0.8007	0.0000	-0.2002	0.3201	-0.1280
RIT:BBH:0295	0.6664	0.3998	0.6000	0.8007	0.5001	-0.2002	-0.0201	0.3080
RIT:BBH:0296	0.5004	0.3333	0.6662	-0.5000	-0.8513	-0.3330	-0.4003	-0.4334
RIT:BBH:0297	0.6664	0.3998	0.6000	-0.8008	0.5001	-0.2002	0.6201	0.0520
RIT:BBH:0298	0.6667	0.4000	0.6000	0.5001	0.2500	-0.2000	-0.0500	0.1700
RIT:BBH:0299	0.4145	0.2929	0.7066	-0.5001	-0.8513	-0.4139	-0.4548	-0.4679
RIT:BBH:0300	0.4145	0.2929	0.7066	0.5001	-0.8513	-0.4139	-0.7476	-0.3821
RIT:BBH:0301	0.6664	0.3998	0.6000	-0.8007	-0.5001	-0.2002	0.0201	-0.3080
RIT:BBH:0302	0.6667	0.4000	0.6000	-0.5001	-0.2500	-0.2000	0.0500	-0.1700
RIT:BBH:0303	0.7140	0.4165	0.5833	0.8007	0.0000	-0.1669	-0.3334	0.1389
RIT:BBH:0304	0.6668	0.4000	0.5999	0.5000	-0.6503	-0.1999	-0.5901	-0.1540
RIT:BBH:0305	0.6667	0.4000	0.6000	-0.5001	0.2500	-0.2000	0.3500	0.0100
RIT:BBH:0306	0.6668	0.4000	0.5999	-0.5001	-0.6503	-0.1999	-0.1901	-0.3140
RIT:BBH:0307	0.6664	0.3998	0.6000	0.8007	0.0000	-0.2002	0.3201	0.1280
RIT:BBH:0308	0.6664	0.3998	0.6000	0.8007	-0.5001	-0.2002	-0.6201	-0.0520
RIT:BBH:0309	0.6667	0.4000	0.6000	0.5000	-0.2500	-0.2000	-0.3500	-0.0100
RIT:BBH:0311	0.6667	0.4000	0.6000	0.0000	0.5001	-0.2000	0.3000	0.1800
RIT:BBH:0312	0.6667	0.4000	0.6000	-0.0000	-0.5001	-0.2000	-0.3000	-0.1800
RIT:BBH:0314	0.5004	0.3333	0.6662	0.5000	0.8513	-0.3330	0.4003	0.4334
RIT:BBH:0316	0.4145	0.2929	0.7066	-0.5001	0.8513	-0.4139	0.7476	0.3821
RIT:BBH:0317	0.7509	0.4283	0.5704	0.9510	0.9532	-0.1422	0.1361	0.4845
RIT:BBH:0318	0.2002	0.1667	0.8327	-0.5000	-0.8514	-0.6664	-0.6252	-0.6042
RIT:BBH:0319	0.7140	0.4165	0.5833	-0.8007	0.0000	-0.1669	0.3334	-0.1389
RIT:BBH:0321	0.2002	0.1667	0.8327	0.5000	-0.8514	-0.6664	-0.7918	-0.5764
RIT:BBH:0322	0.4145	0.2929	0.7066	0.5001	0.8513	-0.4139	0.4548	0.4679
RIT:BBH:0324	1.0000	0.4995	0.4995	0.9017	0.9017	0.0000	-0.0000	0.4500
RIT:BBH:0336	0.4998	0.3332	0.6667	-0.8007	0.0000	-0.3335	0.2668	-0.0889
RIT:BBH:0337	0.2002	0.1667	0.8327	-0.5001	0.8514	-0.6664	0.7918	0.5764
RIT:BBH:0338	0.4998	0.3332	0.6667	0.8006	0.0000	-0.3335	-0.2667	0.0889
RIT:BBH:0339	0.3335	0.2500	0.7496	-0.0000	-0.8009	-0.4998	-0.6001	-0.4500
RIT:BBH:0344	0.6004	0.3750	0.6246	-0.5000	-0.8513	-0.2497	-0.3440	-0.4024

Continued on next page

TABLE III – continued from previous page

Run	q^r	m_1^r/m	m_2^r/m	χ_{1z}^r	χ_{2z}^r	δm_r	S_r/m_r^2	Δ_r/m_r^2
RIT:BBH:0345	0.2002	0.1667	0.8327	0.5001	0.8514	-0.6664	0.6252	0.6042
RIT:BBH:0348	0.6000	0.3750	0.6250	-0.0000	-0.5001	-0.2500	-0.3125	-0.1953
RIT:BBH:0350	0.6001	0.3750	0.6249	-0.5000	-0.6502	-0.2499	-0.2188	-0.3242
RIT:BBH:0352	0.6004	0.3750	0.6245	-0.0000	-0.8513	-0.2497	-0.5314	-0.3320

TABLE IV: The mass and spin of the precessing BHs in Table II after the BHs had time to equilibrate ($t/m = 200$).

Run	q^r	m_1^r/m	m_2^r/m	χ_{1x}^r	χ_{1y}^r	χ_{1z}^r	χ_{2x}^r	χ_{2y}^r	χ_{2z}^r
RIT:BBH:0127	0.7501	0.4284	0.5712	-	-	0.8005	0.5115	0.1815	-0.5887
RIT:BBH:0128	0.5001	0.3332	0.6663	0.0124	0.0059	0.8004	0.6819	0.1550	-0.3901
RIT:BBH:0129	0.3334	0.2499	0.7496	-	-	0.8004	0.7473	0.1250	-0.2596
RIT:BBH:0130	0.7500	0.4284	0.5712	-	-	-0.8007	0.5104	0.1674	0.5937
RIT:BBH:0131	0.5001	0.3332	0.6663	0.0003	-0.0055	-0.8006	0.6686	0.1790	0.4025
RIT:BBH:0132	0.3334	0.2499	0.7496	0.0097	-0.0299	-0.7999	0.7457	0.1224	0.2650
RIT:BBH:0230	0.6670	0.4000	0.5997	-	-	-	-0.5691	-0.0579	-0.5605
RIT:BBH:0231	0.6670	0.4000	0.5997	-	-	-	-0.4404	-0.3553	-0.5667
RIT:BBH:0233	0.6670	0.4000	0.5997	-	-	-	-0.2023	-0.5351	-0.5604
RIT:BBH:0234	0.6670	0.4000	0.5997	-	-	-	0.0675	-0.5711	-0.5573
RIT:BBH:0235	0.6670	0.4000	0.5997	-	-	-	0.3372	-0.4621	-0.5604
RIT:BBH:0236	0.6670	0.4000	0.5997	-	-	-	0.5192	-0.2284	-0.5653
RIT:BBH:0242	0.6670	0.4000	0.5997	-	-	-	0.4585	0.3360	-0.5641
RIT:BBH:0243	0.6670	0.4000	0.5997	-	-	-	0.1980	0.5253	-0.5711
RIT:BBH:0244	0.6670	0.4000	0.5997	-	-	-	-0.5181	0.2330	-0.5645
RIT:BBH:0248	0.6670	0.4000	0.5997	-	-	-	0.5545	0.0630	-0.5744
RIT:BBH:0250	0.6670	0.4000	0.5997	-	-	-	-0.0916	0.5607	-0.5643
RIT:BBH:0251	0.6670	0.4000	0.5997	-	-	-	-0.3355	0.4590	-0.5639
RIT:BBH:0255	0.6670	0.4000	0.5997	-	-	-	0.3986	0.0379	0.6935
RIT:BBH:0256	0.6670	0.4000	0.5997	-	-	-	0.3377	0.2299	0.6887
RIT:BBH:0257	0.6670	0.4000	0.5997	-	-	-	0.1446	0.3677	0.6965
RIT:BBH:0258	0.6670	0.4000	0.5997	-	-	-	-0.0647	0.3934	0.6945
RIT:BBH:0259	0.6670	0.4000	0.5997	-	-	-	-0.2532	0.3151	0.6913
RIT:BBH:0260	0.6670	0.4000	0.5997	-	-	-	-0.3785	0.1469	0.6903
RIT:BBH:0264	0.6670	0.4000	0.5997	-	-	-	0.7956	0.0910	0.0005
RIT:BBH:0266	0.6670	0.4000	0.5997	-	-	-	0.6415	0.4794	-0.0006
RIT:BBH:0267	0.6669	0.4000	0.5998	-	-	-	-0.5020	0.6238	-0.0004
RIT:BBH:0268	0.6670	0.4000	0.5997	-	-	-	-0.7467	0.2894	-0.0027
RIT:BBH:0269	0.6670	0.4000	0.5997	-	-	-	0.6911	0.0897	0.3946
RIT:BBH:0270	0.6670	0.4000	0.5997	-	-	-	0.5501	0.4193	0.4036
RIT:BBH:0271	0.6670	0.4000	0.5997	-	-	-	0.2643	0.6419	0.3992
RIT:BBH:0272	0.6669	0.4000	0.5997	-	-	-	-0.1192	0.6815	0.4031
RIT:BBH:0273	0.6670	0.4000	0.5997	-	-	-	-0.4388	0.5414	0.3943
RIT:BBH:0274	0.6670	0.4000	0.5997	-	-	-	-0.6429	0.2683	0.3949
RIT:BBH:0280	0.6670	0.4000	0.5997	-	-	-	0.2865	0.7477	0.0043
RIT:BBH:0281	0.6669	0.4000	0.5998	-	-	-	-0.1417	0.7880	0.0055

TABLE V: Table of the initial orbital frequency $m\omega_i$, number of orbits to merger, N , and the initial and final eccentricities, e_i and e_f for the spinning cases.

Run	$m\omega_i$	N	e_i	e_f
RIT:BBH:0127	0.0317	5.9	0.0117	0.0022
RIT:BBH:0128	0.0309	6.3	0.0108	0.0033
RIT:BBH:0129	0.0300	7.3	0.0092	0.0010
RIT:BBH:0130	0.0315	6.3	0.0117	0.0013
RIT:BBH:0131	0.0306	7.0	0.0110	0.0039
RIT:BBH:0132	0.0296	8.2	0.0097	0.0044
RIT:BBH:0136	0.0156	22.0	0.0242	0.0009
RIT:BBH:0220	0.0211	8.8	0.0064	0.0024

Continued on next page

TABLE V – continued from previous page

Run	$m\omega_i$	N	e_i	e_f
RIT:BBH:0221	0.0199	14.1	0.0036	0.0015
RIT:BBH:0222	0.0192	23.6	0.0026	0.0006
RIT:BBH:0223	0.0196	11.2	0.0042	0.0011
RIT:BBH:0224	0.0189	29.6	0.0024	0.0006
RIT:BBH:0226	0.0194	20.5	0.0024	0.0009
RIT:BBH:0227	0.0194	13.6	0.0041	0.0011
RIT:BBH:0228	0.0194	13.6	0.0041	0.0012
RIT:BBH:0230	0.0210	9.6	0.0063	0.0012
RIT:BBH:0231	0.0210	9.6	0.0064	0.0010
RIT:BBH:0232	0.0201	8.3	0.0045	0.0016
RIT:BBH:0233	0.0209	9.7	0.0043	0.0015
RIT:BBH:0234	0.0209	9.7	0.0043	0.0011
RIT:BBH:0235	0.0209	9.6	0.0041	0.0017
RIT:BBH:0236	0.0210	9.6	0.0039	0.0014
RIT:BBH:0237	0.0226	7.9	0.0042	0.0019
RIT:BBH:0238	0.0229	6.8	0.0039	0.0020
RIT:BBH:0239	0.0224	8.6	0.0040	0.0017
RIT:BBH:0240	0.0199	8.9	0.0042	0.0014
RIT:BBH:0241	0.0306	6.4	0.0062	0.0029
RIT:BBH:0242	0.0210	9.6	0.0063	0.0012
RIT:BBH:0243	0.0209	9.7	0.0043	0.0015
RIT:BBH:0244	0.0210	9.6	0.0039	0.0019
RIT:BBH:0245	0.0198	10.7	0.0036	0.0001
RIT:BBH:0246	0.0195	18.5	0.0032	0.0009
RIT:BBH:0247	0.0192	16.7	0.0039	0.0008
RIT:BBH:0248	0.0210	9.6	0.0038	0.0012
RIT:BBH:0249	0.0193	13.9	0.0043	0.0010
RIT:BBH:0250	0.0209	9.7	0.0043	0.0017
RIT:BBH:0251	0.0209	9.6	0.0041	0.0017
RIT:BBH:0252	0.0216	14.0	0.0041	0.0013
RIT:BBH:0253	0.0419	6.7	0.0248	0.0038
RIT:BBH:0254	0.0196	10.9	0.0045	0.0012
RIT:BBH:0255	0.0245	10.8	0.0026	0.0023
RIT:BBH:0256	0.0244	10.8	0.0027	0.0016
RIT:BBH:0257	0.0244	10.8	0.0024	0.0016
RIT:BBH:0258	0.0244	10.8	0.0024	0.0016
RIT:BBH:0259	0.0244	10.8	0.0024	0.0014
RIT:BBH:0260	0.0244	10.8	0.0025	0.0014
RIT:BBH:0261	0.0196	11.1	0.0042	0.0011
RIT:BBH:0262	0.0218	12.6	0.0028	0.0009
RIT:BBH:0263	0.0191	16.6	0.0045	0.0010
RIT:BBH:0264	0.0230	9.9	0.0038	0.0013
RIT:BBH:0265	0.0196	11.2	0.0068	0.0010
RIT:BBH:0266	0.0229	9.9	0.0036	0.0019
RIT:BBH:0267	0.0228	9.9	0.0041	0.0017
RIT:BBH:0268	0.0229	9.9	0.0032	0.0013
RIT:BBH:0269	0.0239	10.4	0.0021	0.0016
RIT:BBH:0270	0.0238	10.4	0.0039	0.0019
RIT:BBH:0271	0.0237	10.4	0.0045	0.0020
RIT:BBH:0272	0.0236	10.4	0.0036	0.0018
RIT:BBH:0273	0.0237	10.4	0.0041	0.0016
RIT:BBH:0274	0.0238	10.4	0.0036	0.0013
RIT:BBH:0276	0.0198	9.7	0.0044	0.0018
RIT:BBH:0277	0.0193	14.0	0.0067	0.0011
RIT:BBH:0278	0.0191	25.8	0.0019	0.0008
RIT:BBH:0279	0.0198	9.7	0.0045	0.0019
RIT:BBH:0280	0.0227	10.0	0.0044	0.0018
RIT:BBH:0281	0.0227	10.0	0.0044	0.0024
RIT:BBH:0283	0.0231	6.5	0.0042	0.0033
RIT:BBH:0284	0.0229	7.5	0.0029	0.0020
RIT:BBH:0285	0.0245	14.0	0.0029	0.0011

Continued on next page

TABLE V – continued from previous page

Run	$m\omega_i$	N	e_i	e_f
RIT:BBH:0286	0.0226	8.5	0.0026	0.0012
RIT:BBH:0287	0.0224	9.1	0.0034	0.0018
RIT:BBH:0288	0.0243	15.3	0.0035	0.0010
RIT:BBH:0289	0.0220	11.4	0.0036	0.0009
RIT:BBH:0290	0.0314	3.4	0.0192	0.0083
RIT:BBH:0291	0.0217	13.6	0.0040	0.0010
RIT:BBH:0292	0.0216	14.8	0.0040	0.0012
RIT:BBH:0293	0.0219	11.6	0.0041	0.0011
RIT:BBH:0294	0.0224	8.8	0.0042	0.0015
RIT:BBH:0295	0.0217	13.6	0.0024	0.0011
RIT:BBH:0296	0.0200	9.1	0.0037	0.0014
RIT:BBH:0297	0.0221	10.4	0.0059	0.0011
RIT:BBH:0298	0.0218	12.1	0.0042	0.0011
RIT:BBH:0299	0.0200	9.3	0.0056	0.0012
RIT:BBH:0300	0.0198	10.7	0.0057	0.0010
RIT:BBH:0301	0.0228	7.3	0.0043	0.0026
RIT:BBH:0302	0.0224	8.6	0.0069	0.0018
RIT:BBH:0303	0.0205	13.1	0.0039	0.0013
RIT:BBH:0304	0.0223	9.1	0.0067	0.0014
RIT:BBH:0305	0.0221	10.2	0.0066	0.0015
RIT:BBH:0306	0.0227	7.4	0.0066	0.0023
RIT:BBH:0307	0.0219	11.8	0.0068	0.0014
RIT:BBH:0308	0.0222	10.1	0.0069	0.0016
RIT:BBH:0309	0.0221	10.4	0.0068	0.0014
RIT:BBH:0311	0.0218	12.0	0.0042	0.0011
RIT:BBH:0312	0.0224	8.7	0.0069	0.0018
RIT:BBH:0314	0.0190	18.6	0.0040	0.0008
RIT:BBH:0316	0.0191	18.2	0.0036	0.0007
RIT:BBH:0317	0.0281	10.8	0.0066	0.0010
RIT:BBH:0318	0.0201	11.7	0.0030	0.0007
RIT:BBH:0319	0.0210	9.7	0.0042	0.0014
RIT:BBH:0321	0.0200	12.7	0.0029	0.0011
RIT:BBH:0322	0.0190	20.0	0.0039	0.0008
RIT:BBH:0324	0.0247	12.4	0.0037	0.0012
RIT:BBH:0336	0.0196	12.0	0.0060	0.0009
RIT:BBH:0337	0.0189	28.3	0.0026	0.0004
RIT:BBH:0338	0.0194	14.9	0.0035	0.0012
RIT:BBH:0339	0.0199	10.7	0.0052	0.0008
RIT:BBH:0344	0.0213	7.8	0.0062	0.0011
RIT:BBH:0345	0.0188	29.7	0.0030	0.0005
RIT:BBH:0348	0.0209	9.8	0.0066	0.0014
RIT:BBH:0350	0.0212	8.5	0.0065	0.0014
RIT:BBH:0352	0.0212	8.7	0.0062	0.0016

TABLE VI: The energy radiated, $\delta\mathcal{M}^{IH} = M_{adm} - M_{rem}^{IH}$, and final spin, χ_{rem}^{IH} , as measured using the IH formalism. The error bars are due to variations in the measured mass and spin with time. For aligned systems with final spin antialigned to the initial orbital angular momentum the minus sign is preserved.

Run	$\delta\mathcal{M}^{IH}$	χ_{rem}^{IH}
RIT:BBH:0127	0.047049 ± 0.000002	0.642923 ± 0.000004
RIT:BBH:0128	0.039357 ± 0.000006	0.609307 ± 0.000086
RIT:BBH:0129	0.029840 ± 0.000001	0.607187 ± 0.000012
RIT:BBH:0130	0.051886 ± 0.000001	0.730998 ± 0.000003
RIT:BBH:0131	0.043854 ± 0.000071	0.768088 ± 0.000570
RIT:BBH:0132	0.034965 ± 0.000000	0.756259 ± 0.000002
RIT:BBH:0136	0.049301 ± 0.000002	0.775972 ± 0.000008
RIT:BBH:0220	0.034360 ± 0.000000	0.463421 ± 0.000032
RIT:BBH:0221	0.013239 ± 0.000006	0.104715 ± 0.000006

Continued on next page

TABLE VI – continued from previous page

Run	$\delta\mathcal{M}^{TH}$	χ_{rem}^{TH}
RIT:BBH:0222	0.024213 ± 0.000002	0.697263 ± 0.000030
RIT:BBH:0223	0.043177 ± 0.000003	0.627577 ± 0.000000
RIT:BBH:0224	0.039046 ± 0.000140	0.880312 ± 0.005699
RIT:BBH:0226	0.018361 ± 0.000004	0.427060 ± 0.000001
RIT:BBH:0227	0.053982 ± 0.000003	0.733438 ± 0.000081
RIT:BBH:0228	0.055817 ± 0.000003	0.751804 ± 0.000196
RIT:BBH:0230	0.038221 ± 0.000002	0.555080 ± 0.000038
RIT:BBH:0231	0.037993 ± 0.000002	0.556462 ± 0.000038
RIT:BBH:0232	0.033037 ± 0.000001	0.419364 ± 0.000090
RIT:BBH:0233	0.037722 ± 0.000002	0.558094 ± 0.000038
RIT:BBH:0234	0.037552 ± 0.000002	0.558906 ± 0.000037
RIT:BBH:0235	0.037696 ± 0.000002	0.557694 ± 0.000038
RIT:BBH:0236	0.038129 ± 0.000001	0.555337 ± 0.000040
RIT:BBH:0237	0.037119 ± 0.000001	0.531769 ± 0.000006
RIT:BBH:0238	0.033155 ± 0.000002	0.428593 ± 0.000007
RIT:BBH:0239	0.039182 ± 0.000001	0.542678 ± 0.000004
RIT:BBH:0240	0.034421 ± 0.000003	0.451168 ± 0.000033
RIT:BBH:0241	0.051719 ± 0.000007	0.743552 ± 0.000049
RIT:BBH:0242	0.037993 ± 0.000002	0.556462 ± 0.000038
RIT:BBH:0243	0.037722 ± 0.000002	0.558094 ± 0.000038
RIT:BBH:0244	0.038129 ± 0.000001	0.555336 ± 0.000040
RIT:BBH:0245	0.029791 ± 0.000003	0.374712 ± 0.000000
RIT:BBH:0246	0.016920 ± 0.000004	0.405685 ± 0.000002
RIT:BBH:0247	0.059225 ± 0.000000	0.854389 ± 0.000011
RIT:BBH:0248	0.038220 ± 0.000002	0.555080 ± 0.000037
RIT:BBH:0249	0.055860 ± 0.000004	0.755050 ± 0.000049
RIT:BBH:0250	0.037552 ± 0.000002	0.558906 ± 0.000037
RIT:BBH:0251	0.037696 ± 0.000002	0.557694 ± 0.000037
RIT:BBH:0252	0.079713 ± 0.000012	0.890918 ± 0.000245
RIT:BBH:0253	0.105833 ± 0.000053	0.940241 ± 0.000027
RIT:BBH:0254	0.041832 ± 0.000003	0.605990 ± 0.000026
RIT:BBH:0255	0.063541 ± 0.000001	0.832657 ± 0.000032
RIT:BBH:0256	0.063236 ± 0.000002	0.833626 ± 0.000050
RIT:BBH:0257	0.062808 ± 0.000003	0.834735 ± 0.000094
RIT:BBH:0258	0.062559 ± 0.000003	0.835152 ± 0.000087
RIT:BBH:0259	0.062811 ± 0.000001	0.834240 ± 0.000049
RIT:BBH:0260	0.063373 ± 0.000003	0.832833 ± 0.000088
RIT:BBH:0261	0.043225 ± 0.000002	0.615218 ± 0.000023
RIT:BBH:0262	0.062388 ± 0.000001	0.806245 ± 0.000047
RIT:BBH:0263	0.079755 ± 0.000086	0.885051 ± 0.001694
RIT:BBH:0264	0.048571 ± 0.000002	0.710881 ± 0.000014
RIT:BBH:0265	0.041759 ± 0.000006	0.584610 ± 0.000056
RIT:BBH:0266	0.047876 ± 0.000000	0.713698 ± 0.000001
RIT:BBH:0267	0.047019 ± 0.000001	0.715990 ± 0.000006
RIT:BBH:0268	0.048562 ± 0.000002	0.710338 ± 0.000012
RIT:BBH:0269	0.054878 ± 0.000001	0.792807 ± 0.000012
RIT:BBH:0270	0.055376 ± 0.000001	0.791199 ± 0.000013
RIT:BBH:0271	0.055820 ± 0.000001	0.790455 ± 0.000008
RIT:BBH:0272	0.056897 ± 0.000000	0.787993 ± 0.000005
RIT:BBH:0273	0.057247 ± 0.000001	0.787618 ± 0.000011
RIT:BBH:0274	0.055833 ± 0.000000	0.791237 ± 0.000007
RIT:BBH:0276	0.037611 ± 0.000002	0.530494 ± 0.000037
RIT:BBH:0277	0.057208 ± 0.000003	0.773654 ± 0.000085
RIT:BBH:0278	0.026856 ± 0.000002	0.715530 ± 0.000043
RIT:BBH:0279	0.037334 ± 0.000002	0.521499 ± 0.000062
RIT:BBH:0280	0.047518 ± 0.000001	0.715617 ± 0.000012
RIT:BBH:0281	0.046779 ± 0.000002	0.717849 ± 0.000014
RIT:BBH:0283	0.030805 ± 0.000002	0.383336 ± 0.000002
RIT:BBH:0284	0.019466 ± 0.000003	0.136838 ± 0.000011
RIT:BBH:0285	0.052236 ± 0.000043	0.883435 ± 0.001081
RIT:BBH:0286	0.020768 ± 0.000001	0.172724 ± 0.000017

Continued on next page

TABLE VI – continued from previous page

Run	$\delta\mathcal{M}^{TH}$	χ_{rem}^{TH}
RIT:BBH:0287	0.039013 ± 0.000001	0.539101 ± 0.000036
RIT:BBH:0288	0.060428 ± 0.000149	0.907461 ± 0.001717
RIT:BBH:0289	0.054364 ± 0.000001	0.781275 ± 0.000012
RIT:BBH:0290	0.030423 ± 0.000016	0.350609 ± 0.000009
RIT:BBH:0291	0.068688 ± 0.000005	0.854343 ± 0.000115
RIT:BBH:0292	0.083983 ± 0.000212	0.906306 ± 0.001585
RIT:BBH:0293	0.053790 ± 0.000001	0.773129 ± 0.000003
RIT:BBH:0294	0.039046 ± 0.000002	0.589673 ± 0.000061
RIT:BBH:0295	0.068155 ± 0.000005	0.844768 ± 0.000009
RIT:BBH:0296	0.026874 ± 0.000004	0.308819 ± 0.000001
RIT:BBH:0297	0.047266 ± 0.000001	0.711723 ± 0.000013
RIT:BBH:0298	0.055193 ± 0.000001	0.766060 ± 0.000001
RIT:BBH:0299	0.023398 ± 0.000003	0.233298 ± 0.000026
RIT:BBH:0300	0.025421 ± 0.000009	0.283357 ± 0.000034
RIT:BBH:0301	0.033411 ± 0.000001	0.462101 ± 0.000007
RIT:BBH:0302	0.037663 ± 0.000001	0.555664 ± 0.000026
RIT:BBH:0303	0.054631 ± 0.000001	0.746572 ± 0.000005
RIT:BBH:0304	0.038894 ± 0.000000	0.549270 ± 0.000030
RIT:BBH:0305	0.045062 ± 0.000000	0.679210 ± 0.000010
RIT:BBH:0306	0.033390 ± 0.000001	0.453122 ± 0.000005
RIT:BBH:0307	0.052619 ± 0.000000	0.732976 ± 0.000018
RIT:BBH:0308	0.043136 ± 0.000001	0.613587 ± 0.000039
RIT:BBH:0309	0.044675 ± 0.000001	0.648076 ± 0.000015
RIT:BBH:0311	0.055694 ± 0.000003	0.781539 ± 0.000019
RIT:BBH:0312	0.037596 ± 0.000001	0.540226 ± 0.000029
RIT:BBH:0314	0.073484 ± 0.000049	0.903065 ± 0.000334
RIT:BBH:0316	0.056812 ± 0.000009	0.871082 ± 0.000187
RIT:BBH:0317	0.104701 ± 0.000080	0.942466 ± 0.000058
RIT:BBH:0318	0.011757 ± 0.000002	-0.105807 ± 0.000008
RIT:BBH:0319	0.039589 ± 0.000000	0.589102 ± 0.000053
RIT:BBH:0321	0.012213 ± 0.000001	-0.090347 ± 0.000006
RIT:BBH:0322	0.068114 ± 0.000014	0.906331 ± 0.000200
RIT:BBH:0324	0.099686 ± 0.000022	0.927790 ± 0.001526
RIT:BBH:0336	0.035055 ± 0.000000	0.574463 ± 0.000013
RIT:BBH:0337	0.037908 ± 0.000002	0.895267 ± 0.000044
RIT:BBH:0338	0.043459 ± 0.000001	0.669149 ± 0.000004
RIT:BBH:0339	0.020426 ± 0.000001	0.178243 ± 0.000006
RIT:BBH:0344	0.030016 ± 0.000001	0.370895 ± 0.000005
RIT:BBH:0345	0.041385 ± 0.000010	0.904325 ± 0.000217
RIT:BBH:0348	0.035551 ± 0.000001	0.513676 ± 0.000012
RIT:BBH:0350	0.031769 ± 0.000000	0.428983 ± 0.000007
RIT:BBH:0352	0.031913 ± 0.000001	0.414030 ± 0.000008

-
- [1] F. Pretorius, Phys. Rev. Lett. **95**, 121101 (2005), gr-qc/0507014.
- [2] M. Campanelli, C. O. Lousto, P. Marronetti, and Y. Zlochower, Phys. Rev. Lett. **96**, 111101 (2006), gr-qc/0511048.
- [3] J. G. Baker, J. Centrella, D.-I. Choi, M. Koppitz, and J. van Meter, Phys. Rev. Lett. **96**, 111102 (2006), gr-qc/051103.
- [4] B. P. Abbott *et al.* (Virgo, LIGO Scientific), Phys. Rev. Lett. **116**, 241102 (2016), arXiv:1602.03840 [gr-qc].
- [5] B. Abbott *et al.* (Virgo, LIGO Scientific), Phys. Rev. Lett. **116**, 061102 (2016), arXiv:1602.03837 [gr-qc].
- [6] B. P. Abbott *et al.* (Virgo, LIGO Scientific), Phys. Rev. Lett. **116**, 241103 (2016), arXiv:1606.04855 [gr-qc].
- [7] B. P. Abbott *et al.* (Virgo, LIGO Scientific), Phys. Rev. **X6**, 041015 (2016), arXiv:1606.04856 [gr-qc].
- [8] B. P. Abbott *et al.* (Virgo, LIGO Scientific), Class. Quant. Grav. **34**, 104002 (2017), arXiv:1611.07531 [gr-qc].
- [9] B. P. Abbott *et al.* (Virgo, LIGO Scientific), Phys. Rev. **D94**, 064035 (2016), arXiv:1606.01262 [gr-qc].
- [10] B. P. Abbott *et al.* (Virgo, LIGO Scientific), Phys. Rev. **D93**, 122004 (2016), [Addendum: Phys. Rev.D94,no.6,069903(2016)], arXiv:1602.03843 [gr-qc].
- [11] G. Lovelace *et al.*, Class. Quant. Grav. **33**, 244002 (2016), arXiv:1607.05377 [gr-qc].
- [12] B. P. Abbott *et al.* (Virgo, LIGO Scientific), Phys. Rev. Lett. **116**, 221101 (2016), arXiv:1602.03841 [gr-qc].

- [13] M. Campanelli, C. O. Lousto, H. Nakano, and Y. Zlochower, Phys. Rev. **D79**, 084010 (2009), arXiv:0808.0713 [gr-qc].
- [14] C. O. Lousto, J. Healy, and H. Nakano, Phys. Rev. **D93**, 044031 (2016), arXiv:1506.04768 [gr-qc].
- [15] B. Szilagyi, J. Blackman, A. Buonanno, A. Taracchini, H. P. Pfeiffer, M. A. Scheel, T. Chu, L. E. Kidder, and Y. Pan, Phys. Rev. Lett. **115**, 031102 (2015), arXiv:1502.04953 [gr-qc].
- [16] χ denotes the spin angular momentum of a black hole in units of the square of its mass. The maximum possible spin is $\chi = 1$.
- [17] G. Lovelace, M. A. Scheel, R. Owen, M. Giesler, R. Katebi, B. Szilágyi, T. Chu, N. Demos, D. A. Hemberger, L. E. Kidder, H. P. Pfeiffer, and N. Afshari, Class. Quant. Grav. **32**, 065007 (2015), arXiv:1411.7297 [gr-qc].
- [18] Y. Zlochower, J. Healy, C. O. Lousto, and I. Ruchlin, Phys. Rev. **D96**, 044002 (2017), arXiv:1706.01980 [gr-qc].
- [19] C. O. Lousto and Y. Zlochower, Phys. Rev. Lett. **106**, 041101 (2011), arXiv:1009.0292 [gr-qc].
- [20] U. Sperhake, V. Cardoso, C. D. Ott, E. Schnetter, and H. Witek, Phys. Rev. **D84**, 084038 (2011), arXiv:1105.5391 [gr-qc].
- [21] C. O. Lousto and Y. Zlochower, Phys. Rev. **D88**, 024001 (2013), arXiv:1304.3937 [gr-qc].
- [22] U. Sperhake, V. Cardoso, F. Pretorius, E. Berti, and J. A. Gonzalez, Phys. Rev. Lett. **101**, 161101 (2008), arXiv:0806.1738 [gr-qc].
- [23] M. Shibata, H. Okawa, and T. Yamamoto, Phys. Rev. **D78**, 101501 (2008), arXiv:0810.4735 [gr-qc].
- [24] J. Healy, I. Ruchlin, C. O. Lousto, and Y. Zlochower, Phys. Rev. **D94**, 104020 (2016), arXiv:1506.06153 [gr-qc].
- [25] J. Healy, F. Herrmann, I. Hinder, D. M. Shoemaker, P. Laguna, and R. A. Matzner, Phys. Rev. Lett. **102**, 041101 (2009), arXiv:0807.3292 [gr-qc].
- [26] R. Gold and B. Bruegmann, Phys. Rev. **D88**, 064051 (2013), arXiv:1209.4085 [gr-qc].
- [27] M. Campanelli, C. O. Lousto, and Y. Zlochower, Phys. Rev. **D74**, 041501(R) (2006), gr-qc/0604012.
- [28] M. Hannam, S. Husa, B. Bruegmann, and A. Gopakumar, Phys. Rev. **D78**, 104007 (2008), arXiv:0712.3787 [gr-qc].
- [29] D. A. Hemberger, G. Lovelace, T. J. Loredo, L. E. Kidder, M. A. Scheel, B. Szilágyi, N. W. Taylor, and S. A. Teukolsky, Phys. Rev. **D88**, 064014 (2013), arXiv:1305.5991 [gr-qc].
- [30] J. Healy and C. O. Lousto, Phys. Rev. **D97**, 084002 (2018), arXiv:1801.08162 [gr-qc].
- [31] M. Campanelli, C. O. Lousto, Y. Zlochower, and D. Merritt, Astrophys. J. **659**, L5 (2007), gr-qc/0701164.
- [32] M. Campanelli, C. O. Lousto, Y. Zlochower, and D. Merritt, Phys. Rev. Lett. **98**, 231102 (2007), gr-qc/0702133.
- [33] F. Herrmann, I. Hinder, D. M. Shoemaker, P. Laguna, and R. A. Matzner, Phys. Rev. **D76**, 084032 (2007), arXiv:0706.2541 [gr-qc].
- [34] D. Pollney, C. Reisswig, L. Rezzolla, B. Szilágyi, M. Ansorg, B. Deris, P. Diener, E. N. Dorband, M. Koppitz, A. Nagar, and E. Schnetter, Phys. Rev. **D76**, 124002 (2007), arXiv:0707.2559 [gr-qc].
- [35] J. G. Baker, J. Centrella, D.-I. Choi, M. Koppitz, J. R. van Meter, and M. C. Miller, Astrophys. J. **653**, L93 (2006), arXiv:astro-ph/0603204 [astro-ph].
- [36] J. A. González, M. D. Hannam, U. Sperhake, B. Bruegmann, and S. Husa, Phys. Rev. Lett. **98**, 231101 (2007), gr-qc/0702052.
- [37] J. D. Schnittman, A. Buonanno, J. R. van Meter, J. G. Baker, W. D. Boggs, J. Centrella, B. J. Kelly, and S. T. McWilliams, Phys. Rev. **D77**, 044031 (2008), arXiv:0707.0301 [gr-qc].
- [38] C. O. Lousto and Y. Zlochower, Phys. Rev. Lett. **107**, 231102 (2011), arXiv:1108.2009 [gr-qc].
- [39] C. O. Lousto and J. Healy, Phys. Rev. Lett. **114**, 141101 (2015), arXiv:1410.3830 [gr-qc].
- [40] C. O. Lousto and J. Healy, Phys. Rev. **D93**, 124074 (2016), arXiv:1601.05086 [gr-qc].
- [41] P. Schmidt, M. Hannam, S. Husa, and P. Ajith, Phys. Rev. **D84**, 024046 (2011), arXiv:1012.2879 [gr-qc].
- [42] C. O. Lousto and Y. Zlochower, Phys. Rev. **D89**, 021501 (2014), arXiv:1307.6237 [gr-qc].
- [43] L. Pekowsky, R. O'Shaughnessy, J. Healy, and D. Shoemaker, Phys. Rev. **D88**, 024040 (2013), arXiv:1304.3176 [gr-qc].
- [44] S. Ossokine, M. Boyle, L. E. Kidder, H. P. Pfeiffer, M. A. Scheel, and B. Szilagyi, Phys. Rev. **D92**, 104028 (2015), arXiv:1502.01747 [gr-qc].
- [45] C. O. Lousto and J. Healy, (2018), arXiv:1805.08127 [gr-qc].
- [46] J. Blackman, S. E. Field, M. A. Scheel, C. R. Galley, D. A. Hemberger, P. Schmidt, and R. Smith, Phys. Rev. **D95**, 104023 (2017), arXiv:1701.00550 [gr-qc].
- [47] J. Blackman, S. E. Field, M. A. Scheel, C. R. Galley, C. D. Ott, M. Boyle, L. E. Kidder, H. P. Pfeiffer, and B. Szilagyi, Phys. Rev. **D96**, 024058 (2017), arXiv:1705.07089 [gr-qc].
- [48] V. Varma, S. E. Field, M. A. Scheel, J. Blackman, L. E. Kidder, and H. P. Pfeiffer, (2018), arXiv:1812.07865 [gr-qc].
- [49] B. Aylott *et al.*, Class. Quant. Grav. **26**, 165008 (2009), arXiv:0901.4399 [gr-qc].
- [50] B. Aylott *et al.*, Class. Quant. Grav. **26**, 114008 (2009), arXiv:0905.4227 [gr-qc].
- [51] P. Ajith *et al.*, Class. Quant. Grav. **29**, 124001 (2012), arXiv:1201.5319 [gr-qc].
- [52] J. Aasi *et al.* (LIGO Scientific Collaboration, Virgo Collaboration, NINJA-2 Collaboration), Class. Quant. Grav. **31**, 115004 (2014), arXiv:1401.0939 [gr-qc].
- [53] I. Hinder, A. Buonanno, M. Boyle, Z. B. Etienne, J. Healy, N. K. Johnson-McDaniel, A. Nagar, H. Nakano, Y. Pan, H. P. Pfeiffer, M. Pürer, C. Reisswig, M. A. Scheel, E. Schnetter, U. Sperhake, B. Szilágyi, W. Tichy, B. Wardell, A. Zenginoglu, D. Alic, S. Bernuzzi, T. Bode, B. Brügmann, L. T. Buchman, M. Campanelli, T. Chu, T. Damour, J. D. Grigsby, M. Hannam, R. Haas, D. A. Hemberger, S. Husa, L. E. Kidder, P. Laguna, L. London, G. Lovelace, C. O. Lousto, P. Marronetti, R. A. Matzner, P. Mösta, A. Mroué, D. Müller, B. C. Mundim, A. Nerozzi, V. Paschalidis, D. Pollney, G. Reisswig, L. Rezzolla, S. L. Shapiro, D. Shoemaker, A. Taracchini, N. W. Taylor, S. A. Teukolsky, M. Thierfelder, H. Witek, and Y. Zlochower, Class. Quant. Grav. **31**, 025012 (2014), arXiv:1307.5307 [gr-qc].

- [54] A. H. Mroue, M. A. Scheel, B. Szilagyi, H. P. Pfeiffer, M. Boyle, *et al.*, Phys. Rev. Lett. **111**, 241104 (2013), arXiv:1304.6077 [gr-qc].
- [55] J. Blackman, S. E. Field, C. R. Galley, B. Szilagyi, M. A. Scheel, M. Tiglio, and D. A. Hemberger, Phys. Rev. Lett. **115**, 121102 (2015), arXiv:1502.07758 [gr-qc].
- [56] T. Chu, H. Fong, P. Kumar, H. P. Pfeiffer, M. Boyle, D. A. Hemberger, L. E. Kidder, M. A. Scheel, and B. Szilagyi, Class. Quant. Grav. **33**, 165001 (2016), arXiv:1512.06800 [gr-qc].
- [57] K. Jani, J. Healy, J. A. Clark, L. London, P. Laguna, and D. Shoemaker, Class. Quant. Grav. **33**, 204001 (2016), arXiv:1605.03204 [gr-qc].
- [58] J. Healy, C. O. Lousto, Y. Zlochower, and M. Campanelli, Class. Quant. Grav. **34**, 224001 (2017), arXiv:1703.03423 [gr-qc].
- [59] J. Lange *et al.*, Phys. Rev. **D96**, 104041 (2017), arXiv:1705.09833 [gr-qc].
- [60] Y. Zlochower, J. G. Baker, M. Campanelli, and C. O. Lousto, Phys. Rev. **D72**, 024021 (2005), arXiv:gr-qc/0505055.
- [61] P. Marronetti, W. Tichy, B. Brügmann, J. Gonzalez, and U. Sperhake, Phys. Rev. **D77**, 064010 (2008), arXiv:0709.2160 [gr-qc].
- [62] D. Alic, C. Bona-Casas, C. Bona, L. Rezzolla, and C. Palenzuela, Phys. Rev. **D85**, 064040 (2012), arXiv:1106.2254 [gr-qc].
- [63] T. Nakamura, K. Oohara, and Y. Kojima, Prog. Theor. Phys. Suppl. **90**, 1 (1987).
- [64] M. Shibata and T. Nakamura, Phys. Rev. **D52**, 5428 (1995).
- [65] T. W. Baumgarte and S. L. Shapiro, Phys. Rev. **D59**, 024007 (1998), gr-qc/9810065.
- [66] C. O. Lousto and Y. Zlochower, Phys. Rev. **D77**, 024034 (2008), arXiv:0711.1165 [gr-qc].
- [67] Y. Zlochower, M. Ponce, and C. O. Lousto, Phys. Rev. **D86**, 104056 (2012), arXiv:1208.5494 [gr-qc].
- [68] J. Healy and C. O. Lousto, Phys. Rev. **D95**, 024037 (2017), arXiv:1610.09713 [gr-qc].
- [69] F. Löffler, J. Faber, E. Bentivegna, T. Bode, P. Diener, R. Haas, I. Hinder, B. C. Mundim, C. D. Ott, E. Schnetter, G. Allen, M. Campanelli, and P. Laguna, Class. Quant. Grav. **29**, 115001 (2012), arXiv:1111.3344 [gr-qc].
- [70] Einstein Toolkit home page: <http://einstein toolkit.org>.
- [71] Cactus Computational Toolkit home page: <http://cactuscode.org>.
- [72] E. Schnetter, S. H. Hawley, and I. Hawke, Class. Quant. Grav. **21**, 1465 (2004), gr-qc/0310042.
- [73] J. Thornburg, Class. Quant. Grav. **21**, 743 (2004), gr-qc/0306056.
- [74] O. Dreyer, B. Krishnan, D. Shoemaker, and E. Schnetter, Phys. Rev. **D67**, 024018 (2003), gr-qc/0206008.
- [75] M. Campanelli, C. O. Lousto, Y. Zlochower, B. Krishnan, and D. Merritt, Phys. Rev. **D75**, 064030 (2007), gr-qc/0612076.
- [76] S. Brandt and B. Brügmann, Phys. Rev. Lett. **78**, 3606 (1997), gr-qc/9703066.
- [77] M. Ansorg, B. Brügmann, and W. Tichy, Phys. Rev. **D70**, 064011 (2004), gr-qc/0404056.
- [78] J. Healy, C. O. Lousto, H. Nakano, and Y. Zlochower, Class. Quant. Grav. **34**, 145011 (2017), arXiv:1702.00872 [gr-qc].
- [79] S. Isoyama and H. Nakano, (2017), arXiv:1705.03869 [gr-qc].
- [80] M. Campanelli and C. O. Lousto, Phys. Rev. **D59**, 124022 (1999), arXiv:gr-qc/9811019 [gr-qc].
- [81] C. O. Lousto and Y. Zlochower, Phys. Rev. **D76**, 041502(R) (2007), gr-qc/0703061.
- [82] H. Nakano, J. Healy, C. O. Lousto, and Y. Zlochower, Phys. Rev. **D91**, 104022 (2015), arXiv:1503.00718 [gr-qc].
- [83] M. Babiuc, B. Szilagyi, J. Winicour, and Y. Zlochower, Phys. Rev. **D84**, 044057 (2011), arXiv:1011.4223 [gr-qc].
- [84] J. Healy, C. O. Lousto, and Y. Zlochower, Phys. Rev. **D90**, 104004 (2014), arXiv:1406.7295 [gr-qc].
- [85] J. Healy, C. O. Lousto, and Y. Zlochower, Phys. Rev. **D96**, 024031 (2017), arXiv:1705.07034 [gr-qc].
- [86] H.-S. Cho, E. Ochsner, R. O’Shaughnessy, C. Kim, and C.-H. Lee, Phys. Rev. **D87**, 024004 (2013), arXiv:1209.4494 [gr-qc].
- [87] J. Healy *et al.*, Phys. Rev. **D97**, 064027 (2018), arXiv:1712.05836 [gr-qc].
- [88] DataTables home page: <https://datatables.net>.
- [89] P. Schmidt, I. W. Harry, and H. P. Pfeiffer, (2017), arXiv:1703.01076 [gr-qc].
- [90] J. G. Baker, M. Campanelli, C. Lousto, and R. Takahashi, Phys. Rev. **D65**, 124012 (2002), arXiv:astro-ph/0202469 [astro-ph].
- [91] C. Reisswig and D. Pollney, Class. Quant. Grav. **28**, 195015 (2011), arXiv:1006.1632 [gr-qc].
- [92] Y. Zlochower and C. O. Lousto, Phys. Rev. **D92**, 024022 (2015), arXiv:1503.07536 [gr-qc].
- [93] C. Pankow, P. Brady, E. Ochsner, and R. O’Shaughnessy, Phys. Rev. D **92**, 023002 (2015), arXiv:1502.04370 [gr-qc].
- [94] J. Lange, R. O’Shaughnessy, M. Boyle, J. Calderón Bustillo, M. Campanelli, T. Chu, J. A. Clark, N. Demos, H. Fong, J. Healy, D. A. Hemberger, I. Hinder, K. Jani, B. Khamesra, L. E. Kidder, P. Kumar, P. Laguna, C. O. Lousto, G. Lovelace, S. Ossokine, H. Pfeiffer, M. A. Scheel, D. M. Shoemaker, B. Szilagyi, S. Teukolsky, and Y. Zlochower, Phys. Rev. D **96**, 104041 (2017), arXiv:1705.09833 [gr-qc].
- [95] R. O’Shaughnessy, J. Blackman, and S. E. Field, Classical and Quantum Gravity **34**, 144002 (2017), arXiv:1701.01137 [gr-qc].
- [96] J. Lange, R. O’Shaughnessy, and M. Rizzo, ArXiv e-prints (2018), arXiv:1805.10457 [gr-qc].
- [97] P. Ajith *et al.*, Phys. Rev. Lett. **106**, 241101 (2011), arXiv:0909.2867 [gr-qc].
- [98] C. O. Lousto and Y. Zlochower, Phys. Rev. **D87**, 084027 (2013), arXiv:1211.7099 [gr-qc].
- [99] Weinstein, Eric W. “Hammer-Aitoff Equal-Area Projection.” From MathWorld—A Wolfram Web Resource. <http://mathworld.wolfram.com/Hammer-AitoffEqualAreaProjection.html>.
- [100] [Https://dcc.ligo.org/LIGO-P1800370/public](https://dcc.ligo.org/LIGO-P1800370/public).
- [101] B. P. Abbott *et al.* (LIGO Scientific, Virgo, ASKAP, BOOTES, DES, Fermi GBM, Fermi-LAT, GRAWITA, INTEGRAL, iPTF, InterPlanetary Network, J-GEM, La Silla-QUEST Survey, Liverpool Telescope, LOFAR, MASTER, MAXI, MWA, Pan-STARRS, PESSTO, Pi of the Sky, SkyMapper, Swift, C2PU, TOROS, VISTA), Astrophys. J. **826**, L13 (2016), arXiv:1602.08492 [astro-ph.HE].

- [102] P. Kumar, J. Blackman, S. E. Field, M. Scheel, C. R. Galley, M. Boyle, L. E. Kidder, H. P. Pfeiffer, B. Szilagyi, and S. A. Teukolsky, (2018), arXiv:1808.08004 [gr-qc].
- [103] S. Babak, A. Taracchini, and A. Buonanno, Phys. Rev. **D95**, 024010 (2017), arXiv:1607.05661 [gr-qc].
- [104] M. Hannam, P. Schmidt, A. Bohé, L. Haegel, S. Husa, *et al.*, (2013), arXiv:1308.3271 [gr-qc].
- [105] B. P. Abbott *et al.* (LIGO Scientific, Virgo), (2018), arXiv:1811.12940 [astro-ph.HE].
- [106] E. Barausse, V. Morozova, and L. Rezzolla, Astrophys. J. **758**, 63 (2012), arXiv:1206.3803 [gr-qc].
- [107] L. Rezzolla, E. Barausse, E. N. Dorband, D. Pollney, C. Reisswig, J. Seiler, and S. Husa, Phys. Rev. **D78**, 044002 (2008), arXiv:0712.3541 [gr-qc].
- [108] F. Hofmann, E. Barausse, and L. Rezzolla, Astrophys. J. **825**, L19 (2016), arXiv:1605.01938 [gr-qc].
- [109] X. Jiménez-Forteza, D. Keitel, S. Husa, M. Hannam, S. Khan, and M. Pürrer, Phys. Rev. **D95**, 064024 (2017), arXiv:1611.00332 [gr-qc].
- [110] C. O. Lousto, M. Campanelli, Y. Zlochower, and H. Nakano, Class. Quant. Grav. **27**, 114006 (2010), arXiv:0904.3541 [gr-qc].
- [111] C. O. Lousto and Y. Zlochower, Phys. Rev. **D89**, 104052 (2014), arXiv:1312.5775 [gr-qc].
- [112] D. Keitel *et al.*, Phys. Rev. **D96**, 024006 (2017), arXiv:1612.09566 [gr-qc].
- [113] P. Peters, Phys. Rev. **136**, B1224 (1964).
- [114] A. H. Mroue, H. P. Pfeiffer, L. E. Kidder, and S. A. Teukolsky, Phys. Rev. **D82**, 124016 (2010), arXiv:1004.4697 [gr-qc].